Radiative forcing by super-volcano eruptions

Eirik R. Enger[1], **Rune Graversen**[1], **Audun Theodorsen**[1]

[1]UiT The Arctic University of Norway, Tromsø, Norway

Key Points:

- The linear RF dependence on AOD breaks down for eruptions larger than Mt. Pinatubo
- The RF to AOD ratio has a time-after-eruption dependence on eruption latitude
- Temperature and RF peak values has a linear dependence and reaches an upper limit

Corresponding author: Eirik R. Enger, `eirik.r.enger@uit.no`

Abstract

We investigate the climatic effects of volcanic eruptions spanning from Mt. Pinatubo-sized events to super-volcanoes. The study is based on ensemble simulations in the Community Earth System Model Version 2 (CESM2) climate model using the Whole Atmosphere Community Climate Model Version 6 (WACCM6) atmosphere model. Our analysis focuses on the impact of different SO_2-amount injections on stratospheric aerosol optical depth (AOD), effective radiative forcing (RF), and global temperature anomalies. Unlike the traditional linear models used for smaller eruptions, our results reveal a non-linear relationship between RF and AOD for larger eruptions. We also uncover a notable time-dependent decrease in aerosol forcing efficiency across all eruption magnitudes during the first post-eruption year. In addition, the study reveals that larger as compared to medium-sized eruption events produce a delayed and sharper peak in AOD, and a longer-lasting temperature response while the time evolution of RF remains similar between the two eruption types. When including the results of previous studies, we find that relating SO_2 to any other parameter is inconsistent across models compared to the relationships between AOD, RF, and temperature anomaly. Thus, we expect the largest uncertainty in model codes to relate to the chemistry and physics of SO_2 evolution. Finally, we find that the peak RF approaches a limiting value, and that the peak temperature response follows linearly, effectively bounding the temperature anomaly to at most $\sim -12\,\mathrm{K}$.

Plain Language Summary

Volcanic eruptions can have a significant impact on the Earth's climate. Eruptions large enough that the aerosols they emit reach the stratosphere cause a cooling effect by reflecting sunlight. Typically, an eruption is measured by its impact on the opacity of the stratosphere and the change in the energy balance at the top of the atmosphere. The two measures are often assumed to be linearly related, but the linearity is tested only against eruptions seen in the last two millennia. We use a coupled climate model to simulate the impact of eruptions of sizes up to the largest known eruptions. The smallest eruptions we simulate are still large enough to cause global climate effects. We find a clear non-linear relationship for eruptions larger than the ones seen in the past two millennia. Our simulations and supporting data shows that the eruption latitude significantly influences the development of the relationship between energy imbalance and stratospheric opacity with time after the eruption. Additionally, we find evidence that the peak energy imbalance reaches a limit, and that the peak temperature response follows linearly with the peak energy imbalance, also reaching a limiting value.

1 Introduction

Effective radiative forcing (RF) and stratospheric aerosol optical depth (AOD) are crucial metrics representing the energy imbalance at top-of-the-atmosphere (TOA) and the stratospheric opacity due to aerosol scattering, respectively. They are extensively used to quantify the impact of major volcanic eruptions. The assumption of a linear dependency of RF on AOD is commonly adopted (Myhre et al., 2013; Andersson et al., 2015), and applying such a linear relationship has yielded reasonably accurate estimates in climate model simulations of volcanic eruptions (Mills et al., 2017; Hansen et al., 2005; Gregory et al., 2016; Marshall et al., 2020; Pitari et al., 2016). Yet, a wide spread in the estimated aerosol forcing efficiencies (RF normalised by AOD) exists among studies, spanning approximately from $\sim -15\,\mathrm{Wm^{-2}AOD^{-1}}$ (Pitari et al., 2016) to $\sim -25\,\mathrm{Wm^{-2}AOD^{-1}}$ (Myhre et al., 2013). Additionally, these estimates are predominantly based on small eruptions with AOD values up to at most ~ 0.7.

Although H_2O, N_2, and CO_2 are the most abundant gases emitted by volcanoes (Robock, 2000), sulphur species such as SO_2 provide a greater influence due to the com-

paratively high background concentrations of the former gases in the atmosphere. The transformation of SO_2 molecules through reactions with OH and H_2O leads to the formation of sulphuric acid (H_2SO_4) (Robock, 2000), which scatters sunlight thereby elevating planetary albedo and reducing the RF. As the conversion from SO_2 to H_2SO_4 occurs over weeks (Robock, 2000), the peak RF experiences a slight delay from the eruption's peak SO_2 injection. The lifetime of the H_2SO_4 aerosols in the stratosphere depends on various factors, including latitude (Marshall et al., 2019; Toohey et al., 2019), volcanic plume height (Marshall et al., 2019), aerosol size (Marshall et al., 2019), the quasi-biennial oscillation phase (Pitari et al., 2016) and the season of the year (determining to which hemisphere aerosols are transported) (Toohey et al., 2011, 2019). In the case of tropical eruptions, aerosols are typically transported poleward in the stratosphere and descend back to mid-latitude troposphere within one to two years (Robock, 2000). Upon descending below the tropopause, these aerosols are readily removed by wet deposition (Liu et al., 2012).

Before the current era of significant anthropogenic climate forcing, volcanic eruptions were the primary forcing mechanism dictating Earth's climate variability during the Holocene period (Sigl et al., 2022). Despite this substantial impact, few climate-model experiments have included volcanic forcing when simulating climate evolution during the Holocene (Sigl et al., 2022), likely implying an exaggerated positive forcing (Gregory et al., 2016; Solomon et al., 2011). This absence of persistent cooling is one of several factors that have been suggested to contribute to the common disparity between simulated and observed global warming (Andersson et al., 2015). Despite extensive attention on understanding the way volcanic eruptions influence climate, questions regarding aerosol particle processes—such as growth and creation rates when OH is scarce—remain unanswered (e.g. Robock, 2000; Zanchettin et al., 2019; Marshall et al., 2020, 2022). These processes impact aerosol scattering efficiency and potentially the RF to AOD relationship. Marshall et al. (2020) observe higher aerosol forcing efficiency in post-eruption years 2 and 3 compared to year 1, and attribute this post-eruption increase in aerosol forcing efficiency to strong spatial concentration in the initial year and subsequent distribution of aerosols over a larger area. This spatial redistribution increases the albedo per global mean AOD thereby causing a stronger RF to AOD ratio (Marshall et al., 2020).

Previous studies of both Mt. Pinatubo (Mills et al., 2017; Hansen et al., 2005) and volcanoes within the instrumental era (Gregory et al., 2016) have been used to estimate the relationship between the RF energy imbalance and change in AOD caused by volcanic eruptions. While Myhre et al. (2013) employ a formula scaling RF by AOD to obtain $-25\,\mathrm{Wm^{-2}AOD^{-1}}$, recent literature reports estimates down to $-19.0(5)\,\mathrm{Wm^{-2}AOD^{-1}}$ (Gregory et al., 2016) and $-18.3(10)\,\mathrm{Wm^{-2}AOD^{-1}}$ (Mills et al., 2017). Synthetic volcano simulations in Marshall et al. (2020) yield a scaling factor of $-20.5(2)\,\mathrm{Wm^{-2}AOD^{-1}}$ across an ensemble of 82 simulations featuring varying injection heights and latitudes of volcanic emissions, with injected SO_2 ranging from 10 to 100 $\mathrm{Tg(SO_2)}$.

A similar simulation setup, albeit with notable differences, was conducted by Niemeier and Timmreck (2015), involving an ensemble of 14 levels of injected sulphur spanning between $1\,\mathrm{Tg(S)yr^{-1}}$ ($2\,\mathrm{Tg(SO_2)yr^{-1}}$) and $100\,\mathrm{Tg(S)yr^{-1}}$ ($200\,\mathrm{Tg(SO_2)yr^{-1}}$). These geoengineering simulations maintained continuous sulphur injections, running until a steady sulphur level was achieved. Results indicated an inverse exponential relationship between RF and injected SO_2 rate, converging to $-65\,\mathrm{Wm^{-2}}$ (Eq. 1). Even the 100× Mt. Pinatubo super-volcano simulation by Jones et al. (2005), which obtained a peak RF of $-60\,\mathrm{Wm^{-2}}$, is below the suggested limit of $-65\,\mathrm{Wm^{-2}}$. Moreover, Timmreck et al. (2010) find a peak RF anomaly of $-18\,\mathrm{Wm^{-2}}$ from a 1700 $\mathrm{Tg(SO_2)}$ eruption simulation, which corresponds well with the function estimated by Niemeier and Timmreck (2015) at the given SO_2 level. Several studies have demonstrated a linear relationship of approximately $-20\,\mathrm{Wm^{-2}AOD^{-1}}$ between RF and AOD, although substantial variability exists in the slope among studies (Mills et al., 2017; Hansen et al., 2005; Gregory et al., 2016; Marshall et al., 2020; Pitari

et al., 2016). Moreover, a time-after-eruption dependence on the RF to AOD ratio is found in Marshall et al. (2020), whereas Niemeier and Timmreck (2015) revealed a non-linear relationship between RF and injected SO_2 rate. Thus, a consensus on the relationship between injected SO_2, AOD, and RF has yet to be established.

One avenue that has garnered considerable attention is comparing the magnitude of volcanic or volcano-like forcings to increased CO_2 levels. Several studies explore the connection between volcanic forcing and the climate sensitivity to a doubling of CO_2 (Boer et al., 2007; Marvel et al., 2016; Merlis et al., 2014; Ollila, 2016; Richardson et al., 2019; Salvi et al., 2022; Wigley et al., 2005). The comparison of forcing from volcanoes and CO_2 aims to mitigate the large uncertainty in estimates of the sensitivity of the real climate system. Inferring climate sensitivity from volcanic eruption events has been attempted as a way to constrain the sensitivity (Boer et al., 2007) by assuming that volcanic and CO_2 forcings produce similar feedbacks (Pauling et al., 2023). Earlier studies suggest the potential for constraining equilibrium cilmate sensitivity (ECS) using volcanoes (Bender et al., 2010), provided that ECS is constrained by effective radiative forcing (ERF) rather than instantaneous radiative forcing (IRF), as ERF accounts for rapid atmospheric adjustments in contrast to IRF (Richardson et al., 2019). However, other studies refute this approach, pointing out that different sensitivities of volcanic forcing and CO_2 doubling seem to exist (Douglass et al., 2006), or that constraining the ECS by ERF lacks accuracy due to the precision of climate simulations (Boer et al., 2007; Salvi et al., 2022). Although ERF offers a more suitable indicator of forcing than IRF (Marvel et al., 2016; Richardson et al., 2019), more recent studies conclude that ECS cannot be constrained from volcanic eruption events (Pauling et al., 2023).

Employing eruptions in the medium to super-volcano size enhances the signal-to-noise ratio without necessitating an extensive and computationally expensive ensemble, and as such, is a tempting way to mimic a large ensemble of smaller volcanic eruptions. However, the AOD, RF, and temperature signatures are not necessarily a simple scaling of that of smaller volcanic eruptions. Previous studies have simulated super-volcanoes using AOD as the input forcing, where the AOD was that of Mt. Pinatubo scaled by a factor of one hundred (Jones et al., 2005). This approach may yield incorrect results, both because the peak of the AOD may be too small or too big, but also because the evolution of the AOD could be inappropriate. Likewise, a different AOD evolution may be found from similar size eruptions, but at different latitudes. To investigate this issue, our simulations are based on four levels of injected SO_2 covering three orders of magnitude and the inclusion of one high latitude eruption of the second largest injected SO_2 case.

We conducted ensemble simulations of volcanic eruptions in the Community Earth System Model Version 2 (CESM2) coupled with the Whole Atmosphere Community Climate Model Version 6 (WACCM6). The ensembles span four different levels of injected SO_2: 26 $Tg(SO_2)$, 400 $Tg(SO_2)$, 1629 $Tg(SO_2)$ and 3000 $Tg(SO_2)$. Details regarding the experimental setup are provided in section 2. Our findings reveal non-linear RF to AOD dependencies for medium to super-volcano size eruptions. Additionally, we observe a time-dependent variation in the RF to AOD ratio, detailed in section 3 and discussed in section 4. Furthermore, our data, along with insights from previous studies, suggest that the RF dependency on injected SO_2 identified by Niemeier and Timmreck (2015) acts as a lower boundary. Our conclusions are presented in section 5.

2 Method

2.1 Model

We use the CESM2 (Danabasoglu et al., 2020) in conjunction with the WACCM6 (Gettelman et al., 2019) and the fully dynamical ocean component Parallel Ocean Program version 2 (POP2) (R. Smith et al., 2010; Danabasoglu et al., 2020). The atmosphere

Table 1. Simulations done with the CESM2[a]

Ensemble name	$Tg(SO_2)$	Lat [°N]	Lon [°E]	Alt [km]	Eruption months
C2W↑↑	3000	0	1	18–20	May, Nov
C2WN↑	1629	56	287.7	18–20	Feb, Aug
C2W↑	1629	0	1	18–20	Feb,May,Aug,Nov
C2W−	400	0	1	18–20	Feb,May,Aug,Nov
C2W↓	26	0	1	18–20	Feb,May,Aug,Nov

[a]The ensembles C2WN↑ and C2W↑ have the same eruption magnitude, but while C2W↑ is located at the equator, C2WN↑ is located at a high northern latitude. C2W↑↑, C2W− and C2W↓ are located at the equator, but with different magnitudes compared to C2W↑. The three smallest tropical ensembles have four members, indicated by the number of eruption months, while the northern latitude and the extra large super-volcano ensemble consists of two members.

model was run at a nominal 2° resolution with 70 vertical levels in the middle atmosphere (MA) configuration.

The WACCM6 version employed in the MA configuration uses the three mode version of the Modal Aerosol Module (MAM3) (Gettelman et al., 2019), a simplified and computationally efficient default setting within the Community Atmosphere Model version 5 (CAM5) (Liu et al., 2016), as described in Liu et al. (2012). The MAM3 was developed from MAM7 and features the modes Aitken, accumulation, and coarse (Liu et al., 2016).

2.2 Simulations

Appendix A provides a description of the simulation setup and utilised output variables. Table 1 summarises the simulations, encompassing four SO_2 injection magnitudes and up to four seasons: 15 February, 15 May, 15 August, and 15 November. The magnitudes vary over three orders of magnitude: 26 $Tg(SO_2)$, 400 $Tg(SO_2)$, 1629 $Tg(SO_2)$, and 3000 $Tg(SO_2)$.

The smallest eruption case, C2W↓, is similar in magnitude as compared to events like Mt. Pinatubo (∼ 10–20 $Tg(SO_2)$; Timmreck et al., 2018) and Mt. Tambora (∼ 56.2 $Tg(SO_2)$; Zanchettin et al., 2016). The intermediate case, C2W−, resembles the magnitude of the Samalas eruption in 1257 (∼ 144–170 $Tg(SO_2)$; Vidal et al., 2016), while the second largest and largest eruption cases, C2W↑ and C2W↑↑, is in the likely range of the Young Toba Tuff (YTT) eruption occurring about 72 000 yr ago (100–10 000 $Tg(SO_2)$; Jones et al., 2005). All eruptions were situated at the equator (0 °N, 1 °E) with SO_2 injected between 18 km and 20 km altitude. Collectively, the four tropical eruption cases C2W↓, C2W−, C2W↑, and C2W↑↑ are referred to as C2WTrop. An additional high-latitude eruption ensemble, labelled C2WN↑, of the same injected SO_2 magnitude as C2W↑ was simulated at 56 °N, 287.7 °E with a six-month separation (15 February and 15 August).

3 Results

3.1 Analysis of the time series

Figure 1 presents time series of global mean AOD, RF, and surface air temperature. The black lines represent the medians across the ensembles, while shading indicates the 5th to 95th percentiles. The four distinct forcing magnitudes (C2W↓, C2W−, C2W↑, and C2W↑↑) outlined in table 1 have been used. The time series in Fig. 1 are normalised

by setting the peak value to unity, defined based on the peak of a fit from a Savitzky-Golay filter of 3rd order and a one-year window length (Savitzky & Golay, 1964).

A notable feature across the subfigures of Fig. 1 is the peak occurrence of the C2W↓ case compared to the larger eruption cases. The peak of C2W↓ arrives earlier for both AOD (Fig. 1a) and temperature (Fig. 1c), while the RF time series in Fig. 1b are all indistinguishable. Cases C2W−, C2W↑, and C2W↑↑ are indistinguishable in their temperature development, and while C2W↓ peaks at an earlier time, it decays similarly to the other cases. Interestingly, the same development between C2W− and C2W↑ is not found in the AOD time series. C2W↓ peaks at an earlier time, but also spends more time around the peak and as such decays at a later time post-eruption. Likewise, C2W− has a faster rise and slower decay compared to C2W↑, but where both peak at a similar time. C2W↑ and C2W↑↑ have similar AOD developments, but where C2W↑↑ show a slightly faster decay from the peak.

The timescale of the perturbation of AOD and RF is shorter than that of the temperature. While the AOD and RF time series return to their equilibrium state within roughly three years, the temperature time series remain heavily perturbed three years post-eruption. Even when running the simulations for 20 years post-eruption, the temperature time series are still decaying.

3.2 RF dependency on AOD

We next focus on the development of the AOD and RF time series relative to each other. Similar comparisons were conducted in Gregory et al. (2016, their Fig. 4) and Marshall et al. (2020, their Fig. 1), with RF plotted against AOD. Figure 2 displays annual mean values from the five simulation cases in table 1; the small eruption case (C2W↓) as blue downward-pointing triangles, the intermediate eruption case (C2W−) as orange thick diamonds, the large tropical eruption case (C2W↑) as green upward-pointing triangles, the extra large eruption case (C2W↑↑) as small pink upward-pointing carets, and the large northern hemisphere eruption case (C2WN↑) as brown upward-pointing three-branched twigs. Also shown are the data from Gregory et al. (2016, Fig. 4, black crosses from HadCM3 sstPiHistVol) as grey crosses labelled G16 (described in Appendix B, section B3). Additionally, the estimated peak values from the Mt. Pinatubo and Mt. Tambora eruptions are plotted as a black star and plus, while the peak from the Jones et al. (2005) simulation is shown as a pink square labelled J05. Finally, red circles represent the peak values obtained from the C2W eruption cases. The straight lines are the same as shown by Gregory et al. (2016). The full data range is shown in Fig. 2a while Fig. 2b highlights a narrow range, focusing on the C2W↓ case.

The annual mean data from the Pinatubo-like C2W↓ case in Fig. 2b have RF values as a function of AOD that follow almost the same constant slope as the G16 data. However, in Fig. 2a we observe that the stronger eruptions lead to dissimilar responses in AOD and RF, where C2W− seems to follow close to a -10 slope and C2W↑ is closer to a -5 slope. The peak values (red circles) suggest a non-linear dependence, while within each eruption strength (same colour) the annual mean values fall relatively close to a straight line.

To investigate the time dependence of the ratio between RF and AOD, we present seasonal means of this ratio in Fig. 3. The plot shows the eruption cases given in table 1, as well as the tropical eruptions from Marshall and Smith (2020) (6 of 82 eruptions), labelled M20 and described in Appendix B, section B2. The C2W↑ case is similar to C2W↑↑ as indicated in table 2, but is not shown in the plot to better highlight C2WN↑. In Fig. 3a, lines are linear regression fits to the seasonal means across all ensemble members, summarised in table 2. Shaded regions are the standard deviation around the seasonal means. A similar shading is plotted in Fig. 3b, but where the regression fits have been omitted for clarity. As the AOD and RF time series start from zero, the ratio from the first sea-

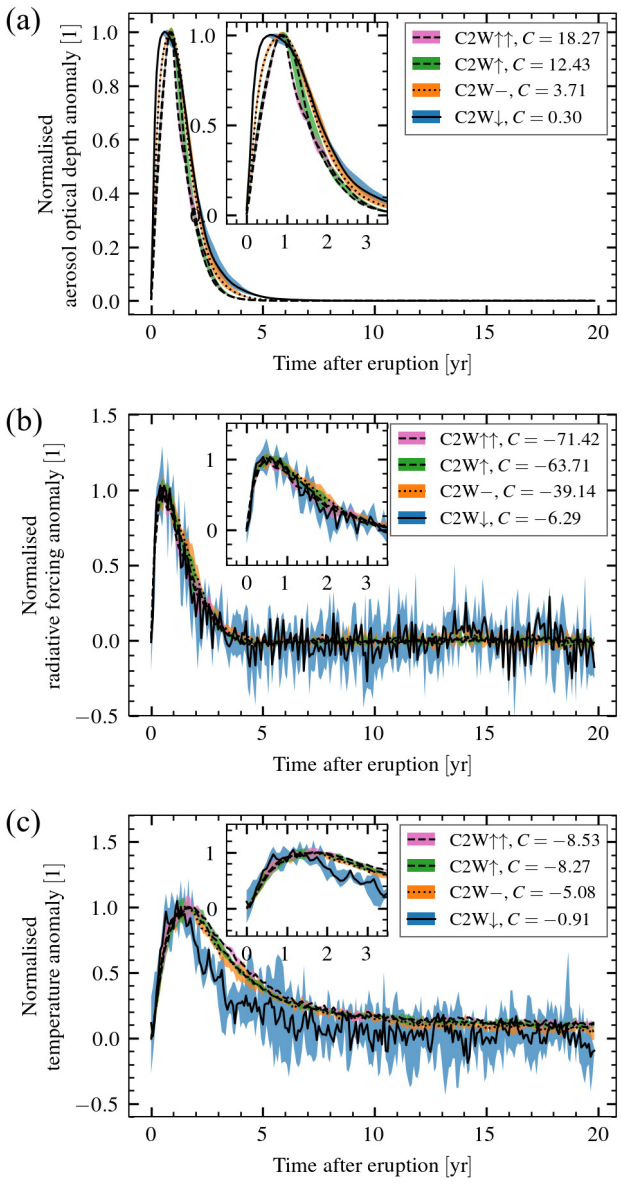

Figure 1. AOD (a), RF (b) and temperature response (c) time series to the four tropical volcanic eruption cases, C2W↓, C2W−, C2W↑, and C2W↑↑. The time series have been normalised to have peak values at unity, where C is the normalisation constant. Black lines indicate the median across the ensembles, while shading marks the 5th and 95th percentiles.

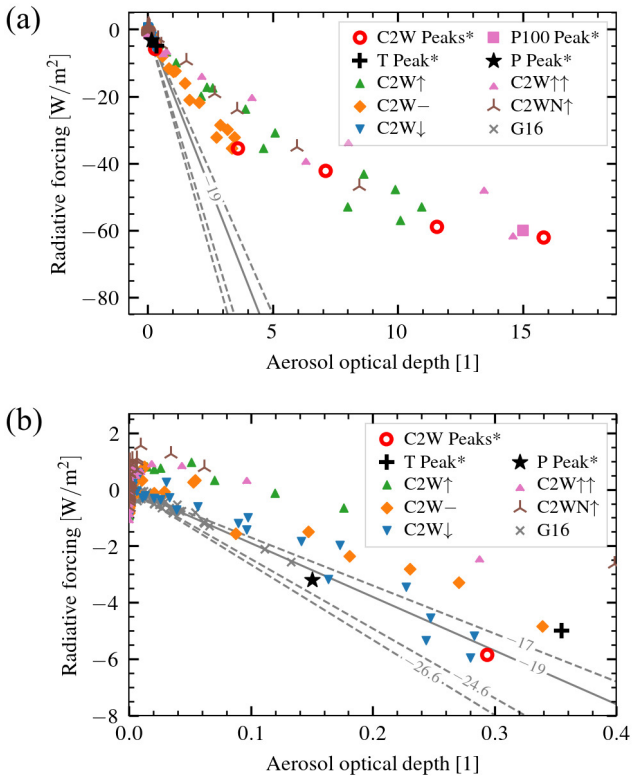

Figure 2. RF as a function of AOD, yearly means. Data from the five simulations listed in table 1 (C2W↓, C2W−, C2W↑, C2WN↑, and C2W↑↑) are shown along with the data from the HadCM3 sstPiHistVol simulation by Gregory et al. (2016) (grey crosses, G16). Also shown are the estimated peak values of the Mt. Pinatubo (black star) and Mt. Tambora (black plus) eruptions. The peak values from the C2W simulations are shown as red circles. Additionally in (a) the simulated super-volcano of Jones et al. (2005) (pink square) is shown. All peak values (as opposed to annual means) have an asterisk (∗) in their label. The grey lines are the same regression fits as in Gregory et al. (2016, Fig. 4), where the solid line is the fit to G16. (b): Zooming in on the smallest AOD values.

Table 2. Slope and standard deviation for the data in Fig. 3[a]

Figure	Ensemble name	Pre-peak	Post-peak
3a	C2WN↑	0.45 ± 1.15	1.51 ± 1.45
	C2W↑↑	3.38 ± 0.97	-2.74 ± 0.77
	C2W↑	3.85 ± 0.52	-3.29 ± 0.60
	C2W−	4.36 ± 0.82	-3.37 ± 0.59
	C2W↓	3.64 ± 2.41	-1.41 ± 3.25
	M20	6.34 ± 1.77	-0.36 ± 1.33
3b	C2WN↑	0.08 ± 0.20	0.27 ± 0.26
	C2W↑↑	0.86 ± 0.25	-0.70 ± 0.19
	C2W↑	0.75 ± 0.10	-0.64 ± 0.12
	C2W−	0.43 ± 0.08	-0.34 ± 0.06
	C2W↓	0.18 ± 0.12	-0.07 ± 0.16
	M20	0.33 ± 0.07	-0.02 ± 0.08

[a]The regression fits in the top half of the table are for Fig. 3a, while the bottom half is for Fig. 3b. The columns "pre-peak" and "post-peak" refer to the two periods as shown in Fig. 3. The ensembles are the same as those given in table 1, in addition to the 6 tropical eruptions from the 82 member ensemble in Marshall et al. (2020).

son is not included. Likewise, after three years both time series are almost fully equilibrated (Fig. 1a,b). The data is further divided into two periods; a pre-peak period where the peak of both the AOD and the RF is included (consisting of the first post-eruption year), and a post-peak period for the decaying part (consisting of the second and third post-eruption years).

Although the ratio changes across the eruption magnitudes, we find that all the tropical cases follow a positive slope during the pre-peak period, as seen in Fig. 3a and described in table 2. The northern latitude case in C2WN↑ shows a much flatter slope compared to C2WTrop and M20. The distinction between the slopes from the tropical and non-tropical cases is perhaps more clear in Fig. 3b and corresponding rows in table 2. Again, C2WN↑ shows an almost flat slope compared to the tropical cases. During the post-peak period, more noise is introduced, but a weak tendency of negative slopes is found among the tropical cases, as well as in the C2WN↑ case up to the last season where the noise is also the largest.

Marshall et al. (2020, their Fig. 1c,d) present results that demonstrate a time-dependent relationship in the conversion between AOD and RF. They obtain an RF to AOD ratio with a negative slope when comparing the first post-eruption year to the second and third. As such, Marshall et al. (2020) find that, on average, the aerosol forcing efficiency increases during the first two to three post-eruption years. This phenomenon is explained by Marshall et al. (2020) as the aerosols initially being spatially confined to the hemisphere where the eruption occurred. Subsequently, during the second and third years, they spread globally, resulting in a higher global-mean albedo per AOD and consequently a stronger RF per AOD ratio with time. However, as noted above, a decrease in aerosol forcing efficiency is found when analysing the M20 data with seasonal resolution during the pre-peak period (first year post-eruption) while constraining the ensemble to only include eruptions within -10 to $10\,^{\circ}$N. The post-peak period shows an increasing aerosol forcing efficiency, and during the full first three post-eruption years (pre-peak and post-peak), both the tropical subset and the full M20 data yield an increasing efficiency, as expected. Likewise, the first three post-eruption years of the C2W−, C2W↑↑, and C2WN↑ cases show a weak negative slope and thus an increasing efficiency, while C2W↓ shows an elevated post-peak ratio as seen in Fig. 3b.

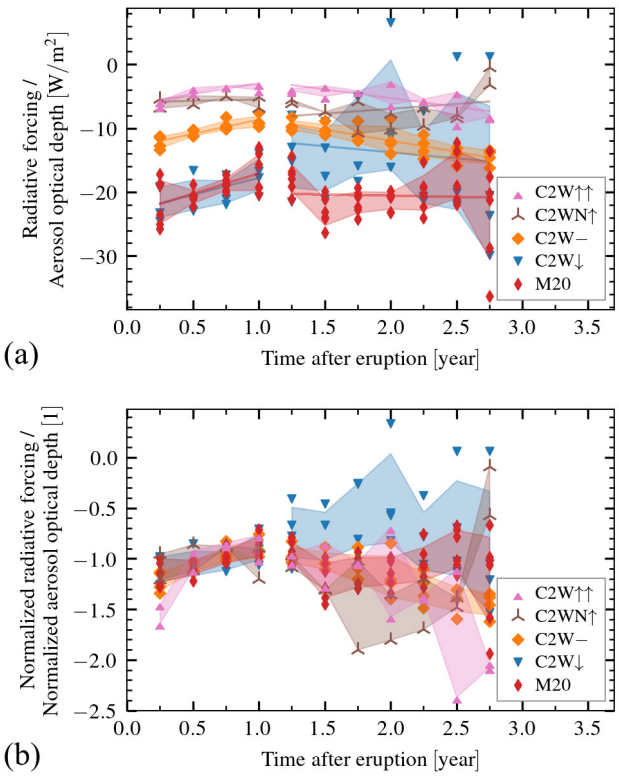

Figure 3. (a): The ratio of RF to AOD, with time-after-eruption on the horizontal axis. Straight lines indicate linear regression fits and are described in table 2, while shaded regions are the standard deviation across the ensembles for each season. Regression fits and shadings are made for the pre-peak and post-peak periods. (b): Same as in (a), but where the underlying AOD and RF time series have been scaled to have peak values at unity. Shown are data from table 1 along with tropical eruptions from M20.

We also note that while the aerosol forcing efficiency is decreasing for tropical M20 data in the pre-peak period, the full dataset shows increasing efficiency. This is in line with what we find from C2WN↑, which is the only eruption case that does not show a clear aerosol forcing efficiency decrease during the pre-peak period.

3.3 Parameter scan

In Fig. 4, we compare the peak values of all investigated CESM2 output parameters against each other as well as to injected SO_2. For our tropical cases (C2WTrop), we observe in Fig. 4a an almost linear yet notably weakening relationship between AOD peak values and injected SO_2. The latitude also plays a role in the magnitude of the AOD perturbation, evident from C2WN↑. This weak yet notable latitude dependence aligns with findings by Marshall et al. (2019), indicating that 72 % of the AOD variance can be attributed to injected SO_2, while latitude accounts for only 16 % of the variance. Peak values from their data (82 simulations) plotted as red thin diamonds display a similar pattern, with AOD exhibiting close to linear dependence on injected SO_2, but with latitude introducing a spread in AOD. Peak values from Mt. Pinatubo (P) and Mt. Tambora (T) are shown for reference, along with peak values from Jones et al. (2005) labelled J05 and Timmreck et al. (2010) labelled T10. The J05 is a simulation of a super-volcano

based on a 100 times scaling of the AOD from Mt. Pinatubo, while T10 is a simulation of the YTT eruption based on SO_2 injections.

In Fig. 4b, RF plotted against injected SO_2 (with the absolute value of RF on the y-axis) indicates a substantial damping effect on RF as injected SO_2 increases for the C2W data, in agreement with results from Otto-Bliesner et al. (2016), labelled OB16. The OB16 data come from a 2500 year long simulation using historic volcanoes as the only external forcing. The analysis details of OB16 can be found in Appendix B, section B1. Despite the model complexity difference, Otto-Bliesner et al. (2016)'s simulations using Community Earth System Model version 1 (CESM1) with a low-top atmosphere (CAM5) produce RFs comparable to our findings.

Niemeier and Timmreck (2015) conducted simulations of continuous sulphur injections up to $200\,\mathrm{Tg(SO_2)yr^{-1}}$ in the ECHAM5's middle atmosphere version (Giorgetta et al., 2006) with aerosol microphysics from HAM (Stier et al., 2005). They observed an RF dependence on SO_2 injection rate following an inverse exponential, which converges to $-65\,\mathrm{Wm^{-2}}$, depicted in Fig. 4b as the stippled pink line labelled N15 and given as;

$$\Delta R_{\mathrm{TOA}} = -65\,\mathrm{Wm^{-2}} e^{-\left(\frac{2246\,\mathrm{Tg(S)yr^{-1}}}{x}\right)^{0.23}}. \quad (1)$$

Both our simulations and OB16 exhibit a notably faster increase than this exponential relationship. The results by N15, on which Eq. 1 is based, are all averages over at least three years of steady sulphur burdens, substantially longer than the time it takes for RF to reach peak values after an eruption. Combined with their lack of a full chemistry model (Niemeier & Timmreck, 2015), a direct comparison between Eq. 1 to peak RF values (occurring about one year post-eruption) may not reflect the same chemical and physical processes. In Eq. 1, x represents S, while the axis shows values of SO_2, thus halving of the SO_2 values on the axis gives the appropriate shape of Eq. 1 as a function of S.

With these caveats in mind, we observe that T10's results closely align with the function described in Eq. 1. Starting with an initial input of $850\,\mathrm{Tg(S)}$ (equivalent to $1700\,\mathrm{Tg(SO_2)}$, representing the YTT eruption), their estimated AOD led to a peak RF of $-18\,\mathrm{Wm^{-2}}$, depicted as a pink filled circle in Fig. 4b. The results from T10 came from a simulation using the MPI-ESM climate model, driven by AOD data from the HAM aerosol model. This alignment likely stems from the utilization of the same aerosol microphysical model in both Timmreck et al. (2010) and Niemeier and Timmreck (2015), as well as the application of similar climate models, MPI-ESM and ECHAM5, respectively. The relationship between climate model families and their implications are further described in Appendix C. Notably, the peak values from M20 fit well within an upper boundary defined by C2WTrop and OB16, and a lower boundary defined by Eq. 1. Eruptions closer to the equator within M20 align with data points near the upper boundary, whereas eruptions at more extreme latitudes tend to yield weaker peak RF values, closer to the lower boundary. Importantly, none of the eruption simulations shown in Fig. 4b exceeded the upper threshold of $-65\,\mathrm{Wm^{-2}}$ as suggested in Eq. 1.

Figure 4c illustrates the response of temperature against injected SO_2. The increase in temperature response with injected SO_2 decreases for higher injected SO_2, showing a similar relationship between C2WTrop, C2WN↑, and OB16. Notably, T10 and J05 exhibit respectively much weaker and much stronger temperature responses to injected SO_2 than C2WTrop. T10 has a maximum temperature anomaly of only $-3.5\,\mathrm{K}$ for their $1700\,\mathrm{Tg(SO_2)}$ eruption, while J05 records a substantially larger maximum temperature anomaly of $-10.7\,\mathrm{K}$. Since the M20 experiment was conducted with prescribed sea-surface temperatures (Marshall et al., 2020), preventing the temperature from being fully perturbed, we do not focus on the M20 data in the temperature plots but include them for completeness.

In Fig. 4d, we revisit the relationship between RF and AOD, focusing on peak values rather than annual and seasonal averages. As previously discussed, the RF to AOD

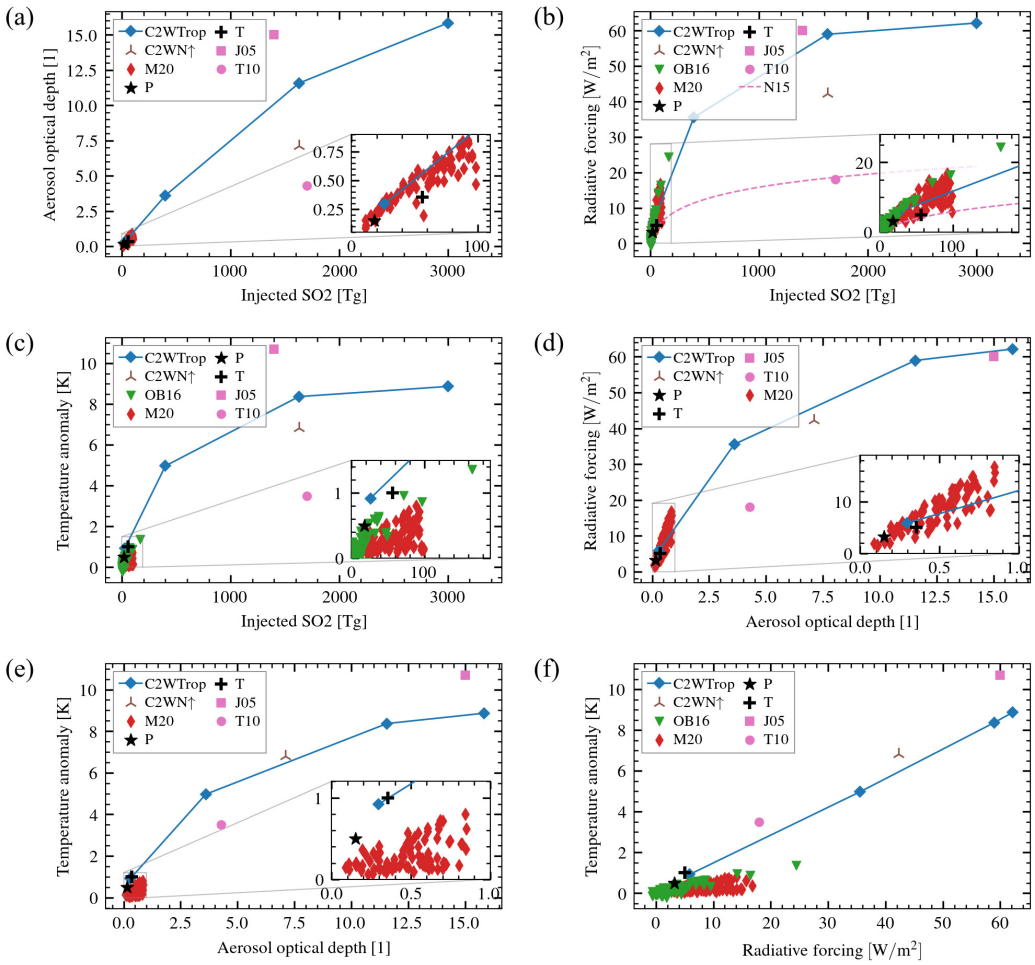

Figure 4. (a) AOD, (b) RF, and (c) temperature anomaly as a function of injected SO_2. (d) RF and (e) temperature anomaly as a function of AOD. (f) Temperature anomaly as a function of RF. Blue diamonds labelled C2WTrop represent tropical cases (C2W↓, C2W−, C2W↑, C2W↑↑), the brown three-branched twig signifies the C2WN↑ case, and green downward triangles denote OB16 data from Otto-Bliesner et al. (2016). The red thin diamonds labelled M20 display the Marshall and Smith (2020) data. Black star and plus indicate Mt. Pinatubo and Mt. Tambora estimates based on observations. The pink square labelled J05 refers to the one-hundred times Mt. Pinatubo super-volcano from Jones et al. (2005), and the pink disk labelled T10 represents the YTT super-volcano from Timmreck et al. (2010). The pink dashed line labelled N15 is from Niemeier and Timmreck (2015), indicating the function in Eq. 1.

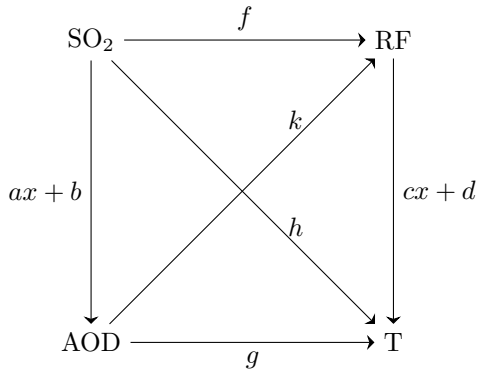

Figure 5. Diagram describing the functional relationships of the parameters shown in Fig. 4.

ratio displays weaker slopes than previous studies, with the C2W peak values not conforming to a linear trend. The relationship between RF and AOD suggests potential substantial dependencies on the model and its input parameters, such as latitude, but most notably to an inherent non-linear RF dependence on AOD. Both the G16 data in Fig. 2 and the J05 data originate from the same climate model. Similarly to what we find from the C2W data, the ratio is much stronger for small eruptions in the industrial era (G16) compared to the super-volcano eruption (J05).

In Fig. 4e, we again find that the response of the C2WTrop data decreases with injected SO_2, this time in temperature anomaly. Additionally, both the C2WN↑ and the J05 cases align well with C2WTrop, with the T10 case following a similar dependence.

Finally, in Fig. 4f, we compare the temperature and RF responses. Both C2WTrop and OB16 show a near-linear relationship between temperature and RF. The C2WTrop data indicate a steeper slope, implying stronger temperature perturbations as compared to OB16. However, potential biases exist in the values from the analysis of OB16, as outlined in Appendix B, section B1. This, along with considerable noise, results in the analysis of OB16 temperature anomalies being less reliable. As in Fig. 4e, the C2WN↑ case along with both the T10 and J05 cases closely follow the temperature to RF dependence of C2WTrop.

The almost linear relationship between AOD and injected SO_2 for the C2WTrop data in Fig. 4a suggests a comparable trend for RF versus injected SO_2 in Fig. 4b, as seen for RF versus AOD in Fig. 4d. For the same reason, we expect Fig. 4e to show a similar pattern for C2WTrop as observed in Fig. 4c.

This relationship, along with the functional relationships between all other parameters shown in Fig. 4, are illustrated in Fig. 5. There, we show that from assuming a linear dependency of AOD on injected SO_2 ($ax+b$), and of temperature on RF ($cx+d$), we must have that f, g, h, and k all have the same functional form, where $f : SO_2 \rightarrow$ RF, g : AOD $\rightarrow$ T, h : SO_2 $\rightarrow$ T, and k : AOD $\rightarrow$ RF. From this, we deduce that $f(x) = k(ax + b)$ and $h(x) = f(cx + d) = g(ax + b)$, and finally that $h(x) = k(acx + ad + b)$, concluding that f, g, h, and k have the same functional form.

3.4 Climate sensitivity estimate

As previously mentioned, the J05 experiment is similar to C2W↑ concerning RF values, yet differ in both AOD and temperature. At the same time J05 is similar to C2W↑↑ in AOD and RF. To investigate this discrepancy, we here conduct a comparison between the J05 climate feedback parameter α (where $s = 1/\alpha$ is the climate sensitivity param-

Table 3. Estimated climate resistance and TCRP[a]

Simulation type	$\rho[\mathrm{Wm^{-2}K^{-1}}]$	$1/\rho$
C2W↑	2.21(5)	0.45(1)
C2W−	2.51(6)	0.40(1)
C2W↓	2.9(6)	0.36(7)
Total	2.5(4)	0.41(5)

[a]Estimates are based on ensembles with four members and $\tau = 20\,\mathrm{yr}$ using Eq. 3.

eter) with our climate resistance, denoted as ρ, and the transient climate response parameter (TCRP) $1/\rho$ (where TCS $= F_{2\times CO_2} \times$ TCRP is the transient climate sensitivity and $F_{2\times CO_2}$ is the forcing due to a doubling of pre-industrial CO_2 concentration). As the forcing of volcanic eruptions typically lasts for about a year, a duration too short for $F = \rho T$ to remain valid, an alternative approach using a time-integral form introduced by Merlis et al. (2014) is applied:

$$\int_0^\tau F\mathrm{d}t = \rho \int_0^\tau T\mathrm{d}t \tag{2}$$

$$\rho = \frac{\int_0^\tau F\mathrm{d}t}{\int_0^\tau T\mathrm{d}t}. \tag{3}$$

If the upper bound of the integral, τ, is sufficiently large, so that the upper ocean heat content is the same at $t = 0$ and $t = \tau$ (Merlis et al. (2014) used $\tau = 15\,\mathrm{yr}$), this approach agrees with $F = \rho T$ for long-term forcing (Gregory et al., 2016). Additionally, we note that the climate resistance and the climate feedback parameter are associated with the ocean heat uptake efficiency (κ) through $\rho = \alpha + \kappa$ (Gregory et al., 2016).

The climate feedback parameter estimated by Jones et al. (2005) is $\alpha \simeq 4\,\mathrm{Wm^{-2}K^{-1}}$, exceeding twice the value obtained by Gregory et al. (2016) in their simulations of Mt. Pinatubo using the same HadCM3 climate model. We determine the climate resistance using the integral-form computation outlined in Eq. 3 and adopting $\tau = 20\,\mathrm{yr}$. The estimated climate resistance from the three tropical simulation cases (with four in each ensemble) converges to $\rho = 2.5(4)\,\mathrm{Wm^{-2}K^{-1}}$, and TCRP values of $1/\rho = 0.41(5)\,\mathrm{KW^{-1}m^2}$, as reported in table 3, and is therefore assumed to be a good estimate of α.

Importantly, our estimate agrees well with G16, while the J05 estimate of $\alpha \simeq 4\,\mathrm{Wm^{-2}K^{-1}}$ is still notably higher. Since the temperature perturbation obtained by J05 was larger than in any of our CESM2 cases, it indicates that the forcing used by J05 must be stronger. The peak value of the J05 RF is similar to the C2W↑ case, and as such, the overall stronger forcing must originate from the development of the forcing time series rather than the peak value.

4 Discussion

Figures 2, 3, and 4d demonstrate that as the AOD exceeds approximately 1.0, the linear RF dependence of approximately $-20\,\mathrm{Wm^{-2}AOD^{-1}}$ no longer holds. The sublinear increase in RF with injected SO_2 in Fig. 4b for large eruptions is consistent with previous results from simulations using similar climate models of smaller historic eruptions (G16) and of super-volcanoes (J05). Such a change in ratio has been attributed to larger eruptions, injecting more SO_2, leading to larger aerosols, and hence less effective radiation scattering, thereby reducing the RF for the same injected SO_2 (English et al., 2013; Timmreck et al., 2010, 2018).

The non-linear relationship between peak RF and AOD values is a strong signature in both Figs. 2 and 3. Across eruptions of the same strength, the ratio stays relatively constant, leading to a close to $-10\,\mathrm{Wm}^{-2}\mathrm{AOD}^{-1}$ slope for C2W− and a $-5\,\mathrm{Wm}^{-2}\mathrm{AOD}^{-1}$ slope for C2W↑ and C2W↑↑. Still, a non-linear development in the RF to AOD ratio is found across all tropical eruptions. Similar to the results of Marshall et al. (2020), we find in C2W−, C2W↑, and C2W↑↑ that the post-peak period (second and third post-eruption years) has a stronger aerosol forcing efficiency compared to the pre-peak period (first post-eruption year). The post-peak period of C2W↓ is elevated as compared to the pre-peak period, resulting in a decreasing aerosol forcing efficiency from the first to the second and third post-eruption years, in contrast to the other tropical eruptions.

Focusing on the pre-peak period, we find tropical eruptions to differ from eruptions at high latitudes. During the pre-peak period, all tropical eruptions show a decreasing aerosol forcing efficiency, while no significant change in the RF to AOD ratio is found from the C2WN↑ case. The full M20 dataset indicates an increasing aerosol forcing efficiency also during the pre-peak period, contrasting the decreasing efficiency found from their tropical eruptions and supporting the latitudinal dependence we find with C2WN↑. While we find a linear relationship to be a useful approximation of RF dependence on AOD for eruptions similar to or smaller than Mt. Pinatubo, additional factors must be considered for larger eruptions. These factors, such as OH scarcity and aerosol growth, influence reflectance and their gravitational pull, substantially impacting both AOD and RF evolution, is highlighted by Timmreck et al. (2010). The large difference in ratio found when comparing eruption magnitudes suggests that injected SO_2 is crucial when estimating the time-average of the RF to AOD ratio. However, latitude and, in particular, aerosol dispersion are more influential in determining the post-eruption evolution of the ratio, particularly during the pre-peak period.

We find that the suggested upper threshold from Eq. 1 is not violated by any eruption simulation, and most notably that the temperature peak value follow the RF trend in reaching a limiting value. The C2WTrop cases follow a close to linear temperature dependency on RF, with the J05, T10, and C2WN↑ aligning close to the same slope. The linear relationship between temperature and RF is the strongest dependence found between the parameters in Fig. 4, and a strong signature across both eruption magnitudes and latitudes, but also across highly different climate models. Thus, from a maximum RF of $-65\,\mathrm{Wm}^{-2}$, we expect temperature anomalies to reach at most $\sim -12\,\mathrm{K}$.

The biggest spread in the data shown in Fig. 4 is found when relating injected SO_2 to any of the three output parameters. As the amount of injected SO_2 increases, both AOD, RF, and temperature across models have a big spread. The AOD to injected SO_2 relationship is consistent within similar models, even when comparing simulations of volcanic eruptions (Timmreck et al., 2010) and continuous injection of SO_2 (Niemeier & Timmreck, 2015), but has a wide spread at high values of injected SO_2 across model families (Figs. 4a,b,c). Comparatively, the RF (Fig. 4d) and temperature (Fig. 4e) as a function of AOD, as well as temperature as a function of RF (Fig. 4f), demonstrate a smaller spread across models. Marshall et al. (2019, 2020, 2021) use a code with seven log-normal modes to simulate aerosol mass and number concentrations, along with an atmosphere-only configuration of the UM-UKCA with prescribed sea-surface temperatures and sea-ice extent (Marshall et al., 2019). This approach is in contrast with CESM2, operating as an Earth System Model, but with a simpler aerosol chemistry model in the MAM3. The family of models to which M20 is based is different from that of C2W and OB16, and also different from the T10 and N15, as described in Appendix C. Based on Fig. 4, we find the model family to be pivotal in determining the estimated AOD and RF magnitudes from injected SO_2, whereas the various models generally demonstrate more consistency in representing RF from AOD.

Timmreck et al. (2010) highlights that for sufficiently large eruptions, OH radicals are too scarce, which limits SO_2 oxidation. The AOD peak in the YTT simulation of T10

occurs six months after Mt. Pinatubo's peak. This aligns with our results, as illustrated in Fig. 1a, where C2W↓ shows an earlier AOD peak compared to C2W−, C2W↑, and C2W↑↑. While the peak RF value of T10 occurs 7–8 months post-eruption, similar to C2W, the J05 peak anomaly occurs one year post-eruption. Additionally, as Jones et al. (2005) obtains a climate feedback parameter larger than both what Gregory et al. (2016) found for the same climate model and larger than the climate resistance obtained here from C2W, we conclude that such a simple approach of scaling the AOD of smaller eruptions to represent larger eruptions is insufficient. Moreover, having a small ensemble of large eruptions to represent smaller eruptions is also insufficient when simulating from injected SO_2, as both AOD and temperature evolution are found to develop differently.

5 Summary and conclusions

We consider five medium to super-volcano sized eruption ensembles and compare them to previously reported results. We find the commonly adopted RF dependence on AOD of $\sim -20\,\mathrm{Wm}^{-2}\mathrm{AOD}^{-1}$ to be representative for Mt. Pinatubo-sized eruptions. Larger eruptions, with one to two orders of magnitude larger injections of SO_2, are found to have an RF dependence on AOD closer to $\sim -10\,\mathrm{Wm}^{-2}\mathrm{AOD}^{-1}$ and $\sim -5\,\mathrm{Wm}^{-2}\mathrm{AOD}^{-1}$. A shallower slope for larger eruptions is also consistent with peak values from previous studies of super-volcanoes.

The time-after-eruption dependence of the ratio between RF and AOD is found to weaken with time, resulting in a decreasing aerosol forcing efficiency in the pre-peak period. The effect is found across all eruption sizes, but only the tropical cases show a clear trend. The high-latitude case displays an almost constant efficiency with time. These results agree with a reanalysis of the tropical data in Marshall and Smith (2020). Thus, these findings provide strong supporting evidence that latitude is generally significant in determining the aerosol forcing efficiency, particularly as a function of time-after-eruption. These findings emphasise the complexity of volcanic impacts on climate, demonstrating significant differences in climatic response depending on eruption magnitude and latitude.

We find that the AOD peak arrives later for larger eruptions than for smaller ones, and also that larger eruptions produce a sharper peak in the AOD time series. The RF time series are similar across all eruption sizes, and while the smallest eruption experiences a faster temperature decay, the larger eruptions produce time series indistinguishable in development for both RF and temperature. Thus, a simple scaling of the AOD or temperature time series from a smaller eruption is insufficient in representing that of larger volcanic eruptions.

Considering injected SO_2 and the peak values of AOD and RF, a large spread is found across model families in Fig. 4. Improving the consistency between model families in how the chemistry and physics of SO_2 and H_2SO_4 are represented is an important step in enhancing the accuracy of simulated volcanic eruptions' influence on climate by models. More simulations of larger volcanic eruptions with injected SO_2 greater than 200 Tg(SO2) would provide useful information for a more precise determination of the RF to AOD ratio in the non-linear regime. This would also serve as a useful test to check if a comparison between SO_2 injection events and continuous SO_2 injection is reasonable. Introducing a spread in latitude similar to the Marshall and Smith (2020) dataset would allow for better comparison between eruptions across all latitudes and the suggested lower limit following Eq. 1, describing a situation of aerosol saturation.

Appendix A Simulation set up and output

Input files used in the simulations were created by modifying the file available at `http://svn.code.sf.net/p/codescripts/code/trunk/ncl/emission/createVolcEruptV3`

`.ncl`, using a Python package available on GitHub at `https://github.com/engeir/volcano-cooking` or through the Python Package Index (PyPI). The package is available both as a library and a Command Line Interface (CLI), and is used to create volcanic eruptions with a specified amount of SO_2 that is injected over six hours at a given latitude, longitude, and altitude. All volcanic SO_2 files are created from a shell script by setting the eruption details in a JSON file that is read by the `volcano-cooking` CLI at a fixed version, ensuring a reproducible experiment setup.

We are using the coupled model version `BWma1850` component setup to run the CESM2, and an accompanying fixed sea-surface temperature version, `fSST1850`, to obtain estimates of the RF. The applied `fSST1850` is not from a standardised component setup but is instead explicitly specified as `1850_CAM60%WCCM_CLM50%BGC-CROP_CICE%PRES_DOCN%DOM_MOSART_CISM2%NOEVOLVE_SWAV_TEST`. The component setup `BWma1850` and `fSST1850` differ in that the latter uses a prescribed sea-ice (`CICE -> CICE%PRES`), a prescribed data ocean (`POP2%ECO%DEP -> DOCN%DOM`) and a stub wave component instead of the full Wave Watch version 3 (`WW3 -> SWAV`).

The important input data used in the model simulations are injected SO_2 in units of teragrams ($Tg(SO_2)$), used to simulate volcanic eruptions. RF is calculated as the combined (short wave and long wave) all-sky TOA energy imbalance, where the CESM2 provide the output variables "net solar flux at the top of the model" (FSNT) and "net longwave flux at the top of the model" (FLNT). Thus, $RF_* = FSNT - FLNT$, and taking the difference between volcanic forcing simulations and a control simulation gives the final estimate of RF ($RF = RF_{VOLC} - RF_{CONTROL}$) (Marshall et al., 2020). The RF calculation is based on `fSST1850`, hence this outline specifically describes how to calculate ERF as opposed to IRF, which instead is the difference between the ERF and the sum of all rapid atmospheric adjustments (Marshall et al., 2020; C. J. Smith et al., 2018). The AOD is obtained from the output variable "stratospheric aerosol optical depth 550 nm day nigth" (AODVISstdn), while global temperature is saved by CESM2 to the variable "reference height temperature" (TREFHT). The analysis of this work is performed using these four variables.

During analysis, one outlier was found in the ensemble representing C2W↓, specifically in the temperature time series. This ensemble member was the February 15, 1850, eruption, which was changed in favor of a February 15, 1851, eruption in the C2W↓, C2W−, and C2W↑ ensembles. For completeness, the February 15, 1850, eruption is still included in the online archive.

Appendix B External data

B1 Otto-Bliesner data analysis

Data from Otto-Bliesner et al. (2016) are the original input data of injected SO_2 as used in their model simulations, along with RF and temperature output data. The injected SO_2 can be found at `https://www.cesm.ucar.edu/working-groups/paleo/simulations/ccsm4-lm`. Only the peak values of the SO_2 dataset were used in the analysis. Output variables are available at `www2.cesm.ucar.edu/models/experiments/LME`.

Since the OB16 dataset contains a five-member ensemble, the final RF and temperature time series used were ensemble means. A single control simulation time series is used to remove seasonal dependence from the temperature, where the control simulation is averaged into a climatology mean. Further, a drift in the temperature is removed by subtracting a linear regression fit. RF has seasonality removed in the Fourier domain.

The time of an eruption is found based on a best attempt at aligning the SO_2 time series with both the RF time series and the temperature time series. The RF and temperature peak values are taken as the value of the time series at the time of an eruption

according to the SO_2 time series. Missing the true peak means the found peaks will be biased towards lower values. However, instances where eruptions occur close in time will contribute a bias to higher values. These biases contribute to a greater uncertainty related to OB16 in Figs. 4b,c,f.

B2 Marshall data analysis

Data used to compute the M20 values were from Marshall and Smith (2020), available at `https://doi.org/10.5285/232164e8b1444978a41f2acf8bbbfe91`. As each file includes a single eruption, peak values of AOD, RF, and temperature were found by applying a Savitzky-Golay filter of third order and one-year window length, and choosing the maximum value (Savitzky & Golay, 1964).

B3 Gregory data analysis

Data used to compute G16 values were kindly provided by Jonathan Gregory (personal communication). The full 160-year-long time series were further analysed by computing annual means.

Appendix C Model families

The model used here was the CESM2 with the WACCM6 atmosphere in the MA configuration. The MA configuration uses the MAM3 (Gettelman et al., 2019), a simplified and computationally efficient default setting within the CAM5 (Liu et al., 2016), as described in Liu et al. (2012). The MAM3 was developed from MAM7, consisting of the seven modes Aitken, accumulation, primary carbon, fine dust, fine sea salt, coarse dust, and coarse sea salt. Instantaneous internal mixing of primary carbonaceous aerosols with secondary aerosols and instantaneous ageing of primary carbonaceous particles are assumed by emitting primary carbon in the accumulation mode (Liu et al., 2016). As dust absorbs water efficiently and is expected to be removed by wet deposition similarly to sea salt, fine dust is merged with fine sea salt into the accumulation mode and coarse dust is merged with coarse sea salt into a coarse mode. The coarse mode will quickly revert to its background state below the tropopause (Liu et al., 2012). Consequently, MAM3 features the three modes Aitken, accumulation, and coarse (Liu et al., 2016).

The CESM2 is an ancestor of CESM1 used by OB16. They belong to a different model family than both the HadCM3 (J05 and G16) and the UM-UKCA (M20), which is an extended version of HadGEM3 (Dhomse et al., 2014), and an ancestor of HadCM3. A third model family is represented through ECHAM5 (N15) and MPI-ESM (T10), where the latter is related to the former via the ECHAM6. A summary of the model code genealogy is in table C1, based on the model code genealogy map created by Kuma et al. (2023).

Acronyms

AODVISstdn "stratospheric aerosol optical depth 550 nm day night"
AOD stratospheric aerosol optical depth
CAM5 Community Atmosphere Model Version 5
CESM1 Community Earth System Model Version 1
CESM2 Community Earth System Model Version 2
ECS equilibrium climate sensitivity
ERF effective radiative forcing
FLNT "net longwave flux at the top of the model"
FSNT "net solar flux at the top of the model"

Table C1. Model code family relations[a]

Family relation	Model name	Data name
CESM1 → CESM1-CAM5 → CESM2	CESM1	OB16
	CESM2	*This contribution*
HadCM3 → HadGEM1 → HadGEM2 → HadGEM3 → UM-UKCA	HadCM3	J05, G16
	UM-UKCA	M20
ECHAM5 → ECHAM6 → MPI-ESM	ECHAM5	N15
	MPI-ESM	T10

[a]Overview of various model codes grouped into families according to the model code genealogy map by Kuma et al. (2023), with each table entry also indicating the specific model code used in the referenced papers of this study.

IRF instantaneous radiative forcing
MAM3 three mode version of the Modal Aerosol Module
MA middle atmosphere
POP2 Parallel Ocean Program Version 2
RF effective radiative forcing
TCRP transient climate response parameter
TOA top-of-the-atmosphere
TREFHT "reference height temperature"
WACCM6 Whole Atmosphere Community Climate Model Version 6
YTT Young Toba Tuff

Open Research Section

The direct output data of CESM2 are too large to be easily archived and transferred. Instead, data generated directly from output fields of CESM2 are made available in a NIRD Research Data Archive (Enger, 2024b), and were generated using scripts available at `https://github.com/engeir/cesm-data-aggregator`. Analysis scripts are available at GitHub (`https://github.com/engeir/code-to-radiative-forcing-by-super-volcano-eruptions`) and is published to Zenodo (Enger, 2024a). Source code used to generate CESM2 input files are available at `https://github.com/engeir/cesm2-volcano-setup`.

Acknowledgments

The simulations were performed on resources provided by Sigma2 — the National Infrastructure for High Performance Computing and Data Storage in Norway.

This work was supported by the Tromsø Research Foundation under Grant Number 19_SG_AT.

Thanks to both Maria Rugenstein and Martin Rypdal for valuable discussions. We would also like to thank the authors of Gregory et al. (2016), Otto-Bliesner et al. (2016), and Marshall and Smith (2020) for making their data available.

References

Andersson, S. M., Martinsson, B. G., Vernier, J.-P., Friberg, J., Brenninkmeijer, C. A. M., Hermann, M., ... Zahn, A. (2015). Significant radiative impact of volcanic aerosol in the lowermost stratosphere. *Nature Communications*,

6, 7692-. Retrieved from https://doi.org/10.1038/ncomms8692 doi: 10.1038/ncomms8692

Bender, F. A. M., Ekman, A. M. L., & Rodhe, H. (2010, October). Response to the eruption of Mount Pinatubo in relation to climate sensitivity in the CMIP3 models. *Climate Dynamics*, *35*(5), 875–886. Retrieved from http://link.springer.com/10.1007/s00382-010-0777-3 doi: 10.1007/s00382-010-0777-3

Boer, G. J., Stowasser, M., & Hamilton, K. (2007, February). Inferring climate sensitivity from volcanic events. *Climate Dynamics*, *28*(5), 481–502. Retrieved from http://link.springer.com/10.1007/s00382-006-0193-x doi: 10.1007/s00382-006-0193-x

Danabasoglu, G., Lamarque, J.-F., Bacmeister, J., Bailey, D. A., DuVivier, A. K., Edwards, J., ... Strand, W. G. (2020). The community earth system model version 2 (CESM2). *Journal of Advances in Modeling Earth Systems*, *12*(2), e2019MS001916. Retrieved from https://agupubs.onlinelibrary.wiley.com/doi/abs/10.1029/2019MS001916 (e2019MS001916 2019MS001916) doi: 10.1029/2019MS001916

Dhomse, S. S., Emmerson, K. M., Mann, G. W., Bellouin, N., Carslaw, K. S., Chipperfield, M. P., ... Thomason, L. W. (2014). Aerosol microphysics simulations of the mt. pinatubo eruption with the um-ukca composition-climate model. *Atmospheric Chemistry and Physics*, *14*(20), 11221–11246. Retrieved from https://acp.copernicus.org/articles/14/11221/2014/ doi: 10.5194/acp-14-11221-2014

Douglass, D. H., Knox, R. S., Pearson, B. D., & Jr., A. C. (2006). Thermocline flux exchange during the pinatubo event. *Geophysical Research Letters*, *33*(19), L19711. Retrieved from https://agupubs.onlinelibrary.wiley.com/doi/abs/10.1029/2006GL026355 doi: 10.1029/2006GL026355

Enger, E. R. (2024a, February). *Accompanying code to 'Radiative forcing by super-volcano eruptions'* [Software]. Zenodo. Retrieved from https://doi.org/10.5281/zenodo.10722164 doi: 10.5281/zenodo.10722164

Enger, E. R. (2024b). *CESM2(WACCM6) single super-volcano simulations* [Dataset]. Norstore. Retrieved from https://doi.org/10.11582/2024.00025 doi: 10.11582/2024.00025

English, J. M., Toon, O. B., & Mills, M. J. (2013). Microphysical simulations of large volcanic eruptions: Pinatubo and toba. *Journal of Geophysical Research: Atmospheres*, *118*(4), 1880–1895. Retrieved from https://agupubs.onlinelibrary.wiley.com/doi/abs/10.1002/jgrd.50196 doi: https://doi.org/10.1002/jgrd.50196

Gettelman, A., Mills, M. J., Kinnison, D. E., Garcia, R. R., Smith, A. K., Marsh, D. R., ... Randel, W. J. (2019). The whole atmosphere community climate model version 6 (WACCM6). *Journal of Geophysical Research: Atmospheres*, *124*(23), 12380–12403. Retrieved from https://agupubs.onlinelibrary.wiley.com/doi/abs/10.1029/2019JD030943 doi: 10.1029/2019JD030943

Giorgetta, M. A., Manzini, E., Roeckner, E., Esch, M., & Bengtsson, L. (2006). Climatology and forcing of the quasi-biennial oscillation in the maecham5 model. *Journal of Climate*, *19*(16), 3882 - 3901. Retrieved from https://journals.ametsoc.org/view/journals/clim/19/16/jcli3830.1.xml doi: 10.1175/JCLI3830.1

Gregory, J. M., Andrews, T., Good, P., Mauritsen, T., & Forster, P. M. (2016, December 01). Small global-mean cooling due to volcanic radiative forcing. *Climate Dynamics*, *47*, 3979–3991. Retrieved from https://doi.org/10.1007/s00382-016-3055-1 doi: 10.1007/s00382-016-3055-1

Hansen, J., Sato, M., Ruedy, R., Nazarenko, L., Lacis, A., Schmidt, G. A., ... Zhang, S. (2005). Efficacy of climate forcings. *Journal of Geophysical Research: Atmospheres*, *110*(D18). Retrieved from https://agupubs.onlinelibrary

.wiley.com/doi/abs/10.1029/2005JD005776 doi: 10.1029/2005JD005776

Jones, G. S., Gregory, J. M., Stott, P. A., Tett, S. F. B., & Thorpe, R. B. (2005, December 01). An AOGCM simulation of the climate response to a volcanic super-eruption . *Climate Dynamics*, *25*(7), 725–738. Retrieved from https://doi.org/10.1007/s00382-005-0066-8 doi: 10.1007/s00382-005-0066-8

Kuma, P., Bender, F. A.-M., & Jönsson, A. R. (2023). Climate model code genealogy and its relation to climate feedbacks and sensitivity. *Journal of Advances in Modeling Earth Systems*, *15*(7), e2022MS003588. Retrieved from https://agupubs.onlinelibrary.wiley.com/doi/abs/10.1029/2022MS003588 (e2022MS003588 2022MS003588) doi: https://doi.org/10.1029/2022MS003588

Liu, X., Easter, R. C., Ghan, S. J., Zaveri, R., Rasch, P., Shi, X., ... Mitchell, D. (2012). Toward a minimal representation of aerosols in climate models: description and evaluation in the community atmosphere model CAM5. *Geoscientific Model Development*, *5*(3), 709–739. Retrieved from https://gmd.copernicus.org/articles/5/709/2012/ doi: 10.5194/gmd-5-709-2012

Liu, X., Ma, P.-L., Wang, H., Tilmes, S., Singh, B., Easter, R. C., ... Rasch, P. J. (2016). Description and evaluation of a new four-mode version of the modal aerosol module (MAM4) within version 5.3 of the community atmosphere model. *Geoscientific Model Development*, *9*(2), 505–522. Retrieved from https://gmd.copernicus.org/articles/9/505/2016/ doi: 10.5194/gmd-9-505-2016

Marshall, L. R., Johnson, J. S., Mann, G. W., Lee, L., Dhomse, S. S., Regayre, L., ... Schmidt, A. (2019). Exploring how eruption source parameters affect volcanic radiative forcing using statistical emulation. *Journal of Geophysical Research: Atmospheres*, *124*(2), 964–985. Retrieved from https://agupubs.onlinelibrary.wiley.com/doi/abs/10.1029/2018JD028675 doi: 10.1029/2018JD028675

Marshall, L. R., Maters, E. C., Schmidt, A., Timmreck, C., Robock, A., & Toohey, M. (2022, May 04). Volcanic effects on climate: recent advances and future avenues. *Bulletin of Volcanology*, *84*(5), 54. Retrieved from https://doi.org/10.1007/s00445-022-01559-3 doi: 10.1007/s00445-022-01559-3

Marshall, L. R., Schmidt, A., Johnson, J. S., Mann, G. W., Lee, L. A., Rigby, R., & Carslaw, K. S. (2021). Unknown eruption source parameters cause large uncertainty in historical volcanic radiative forcing reconstructions. *Journal of Geophysical Research: Atmospheres*, *126*(13), e2020JD033578. Retrieved from https://agupubs.onlinelibrary.wiley.com/doi/abs/10.1029/2020JD033578 (e2020JD033578 2020JD033578) doi: 10.1029/2020JD033578

Marshall, L. R., & Smith, C. J. (2020, September 25). Vol-Clim: UM-UKCA interactive stratospheric aerosol model summary data for perturbed parameter ensemble of volcanic eruptions [dataset]. *Centre for Environmental Data Analysis*. Retrieved from https://dx.doi.org/10.5285/232164e8b1444978a41f2acf8bbbfe91 doi: 10.5285/232164e8b1444978a41f2acf8bbbfe91

Marshall, L. R., Smith, C. J., Forster, P. M., Aubry, T. J., Andrews, T., & Schmidt, A. (2020). Large variations in volcanic aerosol forcing efficiency due to eruption source parameters and rapid adjustments. *Geophysical Research Letters*, *47*(19), e2020GL090241. Retrieved from https://agupubs.onlinelibrary.wiley.com/doi/abs/10.1029/2020GL090241 (e2020GL090241 2020GL090241) doi: 10.1029/2020GL090241

Marvel, K., Schmidt, G. A., Miller, R. L., & Nazarenko, L. S. (2016, April 01). Implications for climate sensitivity from the response to individual forcings. *Nature Climate Change*, *6*(4), 386–389. Retrieved from https://doi.org/10.1038/nclimate2888 doi: 10.1038/nclimate2888

Merlis, T. M., Held, I. M., Stenchikov, G. L., Zeng, F., & Horowitz, L. W. (2014).

Constraining transient climate sensitivity using coupled climate model simulations of volcanic eruptions. *Journal of Climate*, *27*(20), 7781–7795. Retrieved from https://journals.ametsoc.org/view/journals/clim/27/20/jcli-d-14-00214.1.xml doi: 10.1175/JCLI-D-14-00214.1

Mills, M. J., Richter, J. H., Tilmes, S., Kravitz, B., MacMartin, D. G., Glanville, A. A., ... Kinnison, D. E. (2017). Radiative and chemical response to interactive stratospheric sulfate aerosols in fully coupled CESM1(WACCM). *Journal of Geophysical Research: Atmospheres*, *122*(23), 13,061–13,078. Retrieved from https://agupubs.onlinelibrary.wiley.com/doi/abs/10.1002/2017JD027006 doi: 10.1002/2017JD027006

Myhre, G., Shindell, D., Bréon, F.-M., Collins, W., Fuglestvedt, J., Huang, J., ... Zhang, H. (2013). Anthropogenic and natural radiative forcing. In T. F. Stocker et al. (Eds.), *Climate change 2013: The physical science basis. contribution of working group i to the fifth assessment report of the intergovernmental panel on climate change* (pp. 659–740). Cambridge, UK: Cambridge University Press. doi: 10.1017/CBO9781107415324.018

Niemeier, U., & Timmreck, C. (2015, August). What is the limit of climate engineering by stratospheric injection of SO2 ? *Atmospheric Chemistry and Physics*, *15*(16), 9129–9141. Retrieved from https://doi.org/10.5194%2Facp-15-9129-2015 doi: 10.5194/acp-15-9129-2015

Ollila, A. (2016, 02). Climate sensitivity parameter in the test of the mount pinatubo eruption. *Physical Science International Journal,*, *9*, 1–14. doi: 10.9734/PSIJ/2016/23242

Otto-Bliesner, B. L., Brady, E. C., Fasullo, J., Jahn, A., Landrum, L., Stevenson, S., ... Strand, G. (2016). Climate variability and change since 850 CE: An ensemble approach with the community earth system model. *Bulletin of the American Meteorological Society*, *97*(5), 735–754. Retrieved from https://journals.ametsoc.org/view/journals/bams/97/5/bams-d-14-00233.1.xml doi: 10.1175/BAMS-D-14-00233.1

Pauling, A. G., Bitz, C. M., & Armour, K. C. (2023). The climate response to the Mt. Pinatubo eruption does not constrain climate sensitivity. *Geophysical Research Letters*, *50*(7), e2023GL102946. Retrieved from https://agupubs.onlinelibrary.wiley.com/doi/abs/10.1029/2023GL102946 (e2023GL102946 2023GL102946) doi: 10.1029/2023GL102946

Pitari, G., Genova, G. D., Mancini, E., Visioni, D., Gandolfi, I., & Cionni, I. (2016). Stratospheric aerosols from major volcanic eruptions: A composition-climate model study of the aerosol cloud dispersal and e-folding time. *Atmosphere*, *7*(6). Retrieved from https://www.mdpi.com/2073-4433/7/6/75 doi: 10.3390/atmos7060075

Richardson, T. B., Forster, P. M., Smith, C. J., Maycock, A. C., Wood, T., Andrews, T., ... Watson-Parris, D. (2019). Efficacy of climate forcings in PDRMIP models. *Journal of Geophysical Research: Atmospheres*, *124*(23), 12824–12844. Retrieved from https://agupubs.onlinelibrary.wiley.com/doi/abs/10.1029/2019JD030581 doi: 10.1029/2019JD030581

Robock, A. (2000). Volcanic eruptions and climate. *Reviews of Geophysics*, *38*(2), 191–219. Retrieved from https://agupubs.onlinelibrary.wiley.com/doi/abs/10.1029/1998RG000054 doi: 10.1029/1998RG000054

Salvi, P., Ceppi, P., & Gregory, J. M. (2022). Interpreting differences in radiative feedbacks from aerosols versus greenhouse gases. *Geophysical Research Letters*, *49*(8), e2022GL097766. Retrieved from https://agupubs.onlinelibrary.wiley.com/doi/abs/10.1029/2022GL097766 (e2022GL097766 2022GL097766) doi: 10.1029/2022GL097766

Savitzky, A., & Golay, M. J. E. (1964). Smoothing and differentiation of data by simplified least squares procedures. *Analytical Chemistry*, *36*(8), 1627-1639. Retrieved from https://doi.org/10.1021/ac60214a047 doi:

10.1021/ac60214a047

Sigl, M., Toohey, M., McConnell, J. R., Cole-Dai, J., & Severi, M. (2022). Volcanic stratospheric sulfur injections and aerosol optical depth during the holocene (past 11 500 years) from a bipolar ice-core array. *Earth System Science Data*, *14*(7), 3167–3196. Retrieved from https://essd.copernicus.org/articles/14/3167/2022/ doi: 10.5194/essd-14-3167-2022

Smith, C. J., Kramer, R. J., Myhre, G., Forster, P. M., Soden, B. J., Andrews, T., ... Watson-Parris, D. (2018). Understanding rapid adjustments to diverse forcing agents. *Geophysical Research Letters*, *45*(21), 12,023-12,031. Retrieved from https://agupubs.onlinelibrary.wiley.com/doi/abs/10.1029/2018GL079826 doi: https://doi.org/10.1029/2018GL079826

Smith, R., Jones, P., Briegleb, B., Bryan, F., Danabasoglu, G., Dennis, J., ... Yeager, S. (2010, 03 23). The parallel ocean program (POP) reference manual. *LAUR-10-01853*. Retrieved from https://www.cesm.ucar.edu/models/cesm1.0/pop2/doc/sci/POPRefManual.pdf

Solomon, S., Daniel, J. S., Neely, R. R., Vernier, J.-P., Dutton, E. G., & Thomason, L. W. (2011). The persistently variable "background" stratospheric aerosol layer and global climate change. *Science*, *333*(6044), 866-870. Retrieved from https://www.science.org/doi/abs/10.1126/science.1206027 doi: 10.1126/science.1206027

Stier, P., Feichter, J., Kinne, S., Kloster, S., Vignati, E., Wilson, J., ... Petzold, A. (2005). The aerosol-climate model echam5-ham. *Atmospheric Chemistry and Physics*, *5*(4), 1125–1156. Retrieved from https://acp.copernicus.org/articles/5/1125/2005/ doi: 10.5194/acp-5-1125-2005

Timmreck, C., Graf, H.-F., Lorenz, S. J., Niemeier, U., Zanchettin, D., Matei, D., ... Crowley, T. J. (2010). Aerosol size confines climate response to volcanic supereruptions. *Geophysical Research Letters*, *37*(24). Retrieved from https://agupubs.onlinelibrary.wiley.com/doi/abs/10.1029/2010GL045464 doi: 10.1029/2010GL045464

Timmreck, C., Mann, G. W., Aquila, V., Hommel, R., Lee, L. A., Schmidt, A., ... Weisenstein, D. (2018). The interactive stratospheric aerosol model intercomparison project (ISA- MIP): motivation and experimental design. *Geoscientific Model Development*, *11*(7), 2581–2608. Retrieved from https://gmd.copernicus.org/articles/11/2581/2018/ doi: 10.5194/gmd-11-2581-2018

Toohey, M., Krüger, K., Niemeier, U., & Timmreck, C. (2011). The influence of eruption season on the global aerosol evolution and radiative impact of tropical volcanic eruptions. *Atmospheric Chemistry and Physics*, *11*(23), 12351–12367. Retrieved from https://acp.copernicus.org/articles/11/12351/2011/ doi: 10.5194/acp-11-12351-2011

Toohey, M., Krüger, K., Schmidt, H., Timmreck, C., Sigl, M., Stoffel, M., & Wilson, R. (2019, February 01). Disproportionately strong climate forcing from extratropical explosive volcanic eruptions. *Nature Geoscience*, *12*(2), 100–107. Retrieved from https://doi.org/10.1038/s41561-018-0286-2 doi: 10.1038/s41561-018-0286-2

Vidal, C. M., Métrich, N., Komorowski, J.-C., Pratomo, I., Michel, A., Kartadinata, N., ... Lavigne, F. (2016, October). The 1257 samalas eruption (lombok, indonesia): the single greatest stratospheric gas release of the common era. *Scientific Reports*, *6*(1). Retrieved from http://dx.doi.org/10.1038/srep34868 doi: 10.1038/srep34868

Wigley, T. M. L., Ammann, C. M., Santer, B. D., & Raper, S. C. B. (2005). Effect of climate sensitivity on the response to volcanic forcing. *Journal of Geophysical Research: Atmospheres*, *110*(D9). Retrieved from https://agupubs.onlinelibrary.wiley.com/doi/abs/10.1029/2004JD005557 doi: 10.1029/2004JD005557

Zanchettin, D., Khodri, M., Timmreck, C., Toohey, M., Schmidt, A., Gerber, E. P., ... Tummon, F. (2016). The model intercomparison project on the climatic response to volcanic forcing (volMIP): experimental design and forcing input data for CMIP6. *Geoscientific Model Development*, *9*(8), 2701–2719. Retrieved from `https://gmd.copernicus.org/articles/9/2701/2016/` doi: 10.5194/gmd-9-2701-2016

Zanchettin, D., Timmreck, C., Toohey, M., Jungclaus, J. H., Bittner, M., Lorenz, S. J., & Rubino, A. (2019). Clarifying the relative role of forcing uncertainties and initial-condition unknowns in spreading the climate response to volcanic eruptions. *Geophysical Research Letters*, *46*(3), 1602–1611. Retrieved from `https://agupubs.onlinelibrary.wiley.com/doi/abs/10.1029/2018GL081018` doi: 10.1029/2018GL081018

Figure 1.

(a)

Normalised aerosol optical depth anomaly [1]

C2W↑↑, $C = 18.27$
C2W↑, $C = 12.43$
C2W−, $C = 3.71$
C2W↓, $C = 0.30$

Time after eruption [yr]

(b)

Normalised radiative forcing anomaly [1]

C2W↑↑, $C = -71.42$
C2W↑, $C = -63.71$
C2W−, $C = -39.14$
C2W↓, $C = -6.29$

Time after eruption [yr]

(c)

Normalised temperature anomaly [1]

C2W↑↑, $C = -8.53$
C2W↑, $C = -8.27$
C2W−, $C = -5.08$
C2W↓, $C = -0.91$

Time after eruption [yr]

Figure 2.

(a)

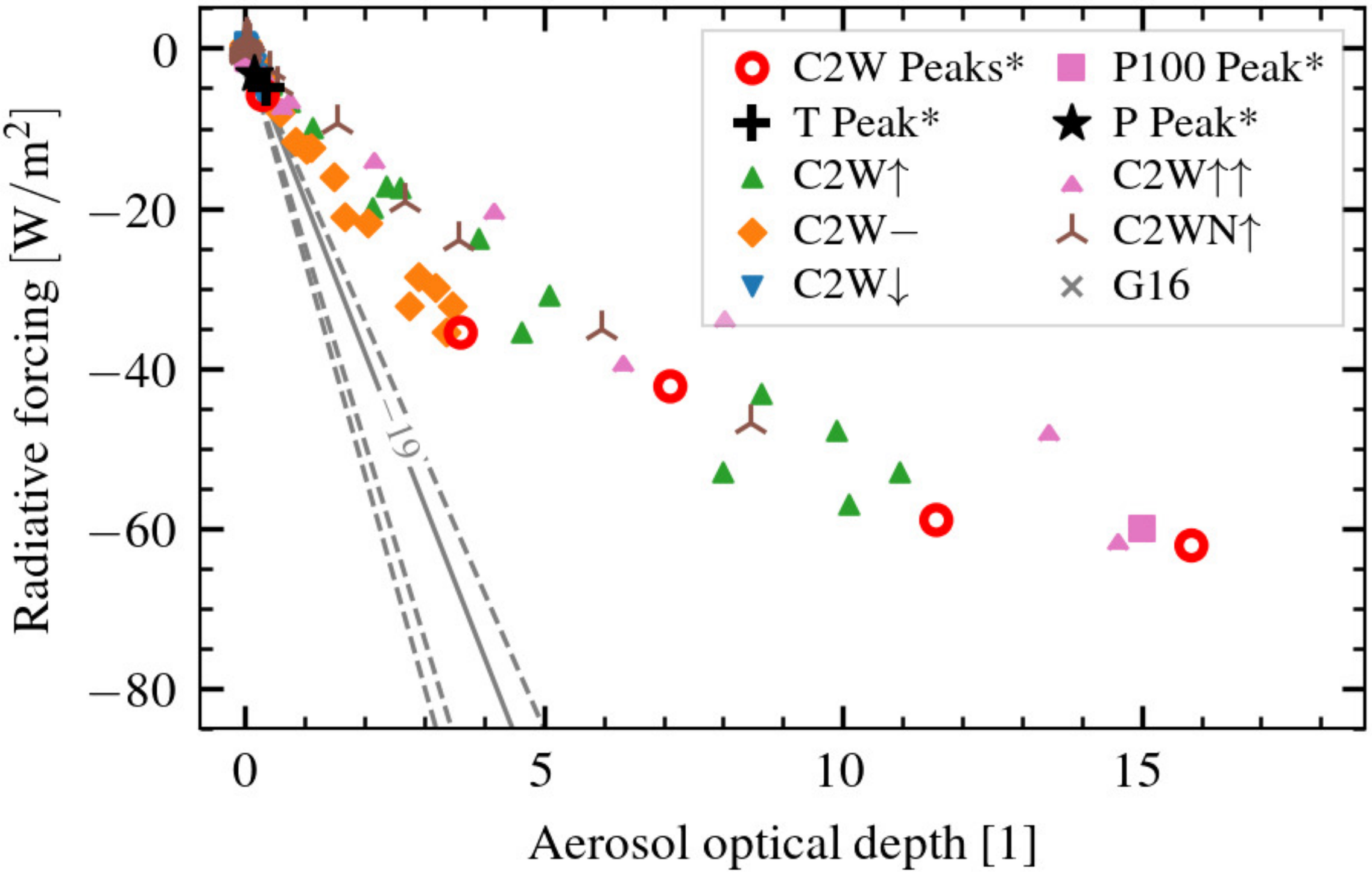
C2W Peaks*
P100 Peak*
T Peak*
P Peak*
C2W↑
C2W↑↑
C2W−
C2WN↑
C2W↓
G16
−19
Radiative forcing [W/m²]
0
−20
−40
−60
−80
0
5
10
15
Aerosol optical depth [1]

(b)

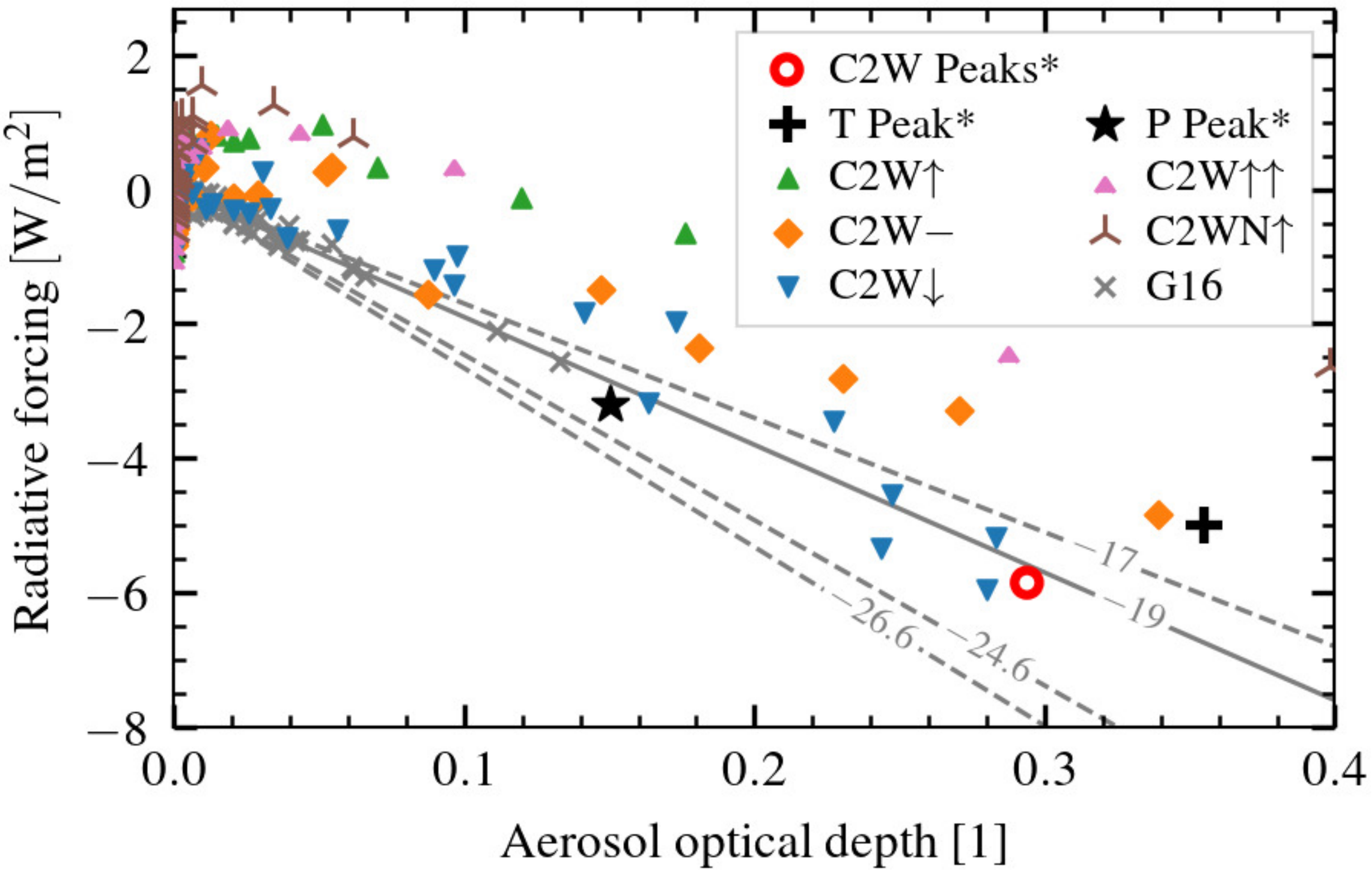
C2W Peaks*
T Peak*
P Peak*
C2W↑
C2W↑↑
C2W−
C2WN↑
C2W↓
G16
−17
−19
−24.6
−26.6
Radiative forcing [W/m²]
2
0
−2
−4
−6
−8
0.0
0.1
0.2
0.3
0.4
Aerosol optical depth [1]

Figure 3.

Radiative forcing / Aerosol optical depth [W/m^2]

0
−10
−20
−30

0.0 0.5 1.0 1.5 2.0 2.5 3.0 3.5

Time after eruption [year]

C2W↑↑
C2WN↑
C2W−
C2W↓
M20

(a)

Normalized radiative forcing / Normalized aerosol optical depth [1]

0.0
−0.5
−1.0
−1.5
−2.0
−2.5

0.0 0.5 1.0 1.5 2.0 2.5 3.0 3.5

Time after eruption [year]

C2W↑↑
C2WN↑
C2W−
C2W↓
M20

(b)

Figure 4.

(a)

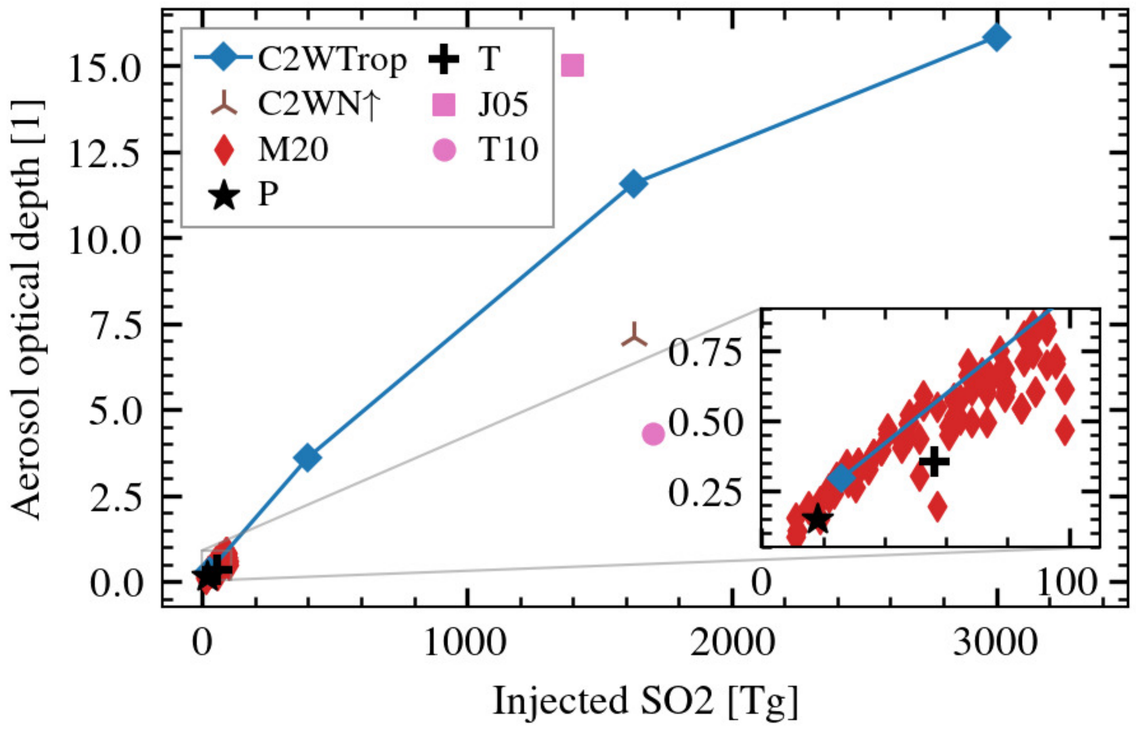
C2WTrop
C2WN↑
M20
P
T
J05
T10
Aerosol optical depth [1]
Injected SO2 [Tg]

(b)

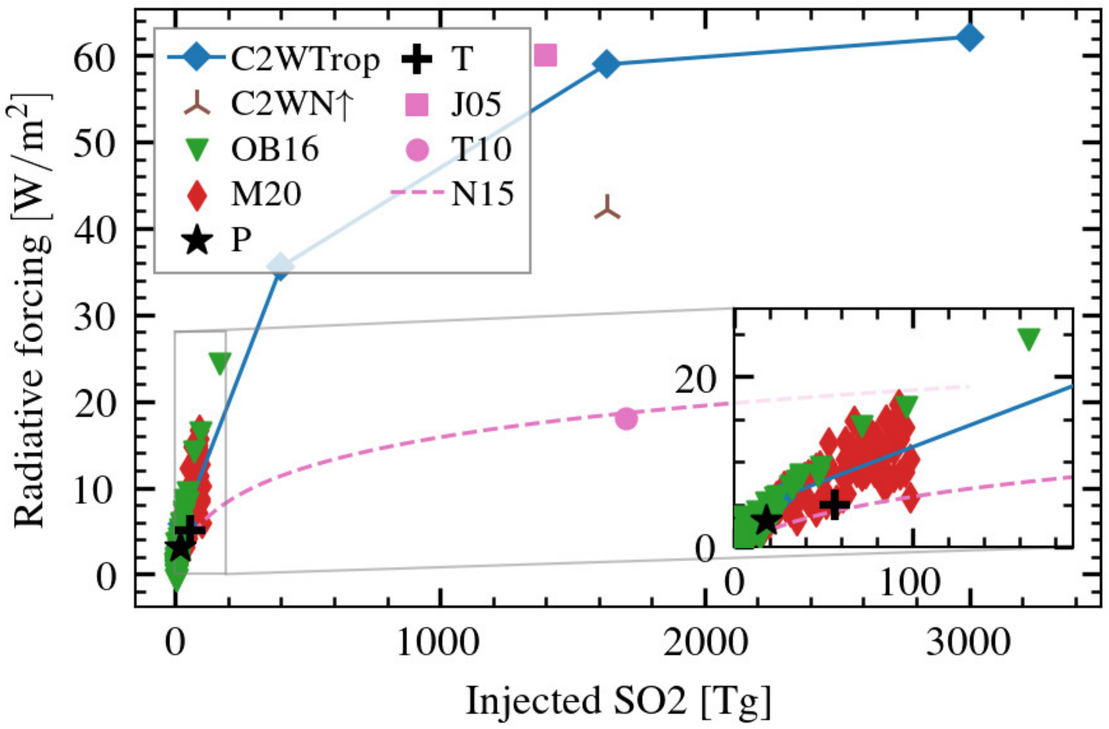
C2WTrop
C2WN↑
OB16
M20
P
T
J05
T10
N15
Radiative forcing [W/m^2]
Injected SO2 [Tg]

(c)

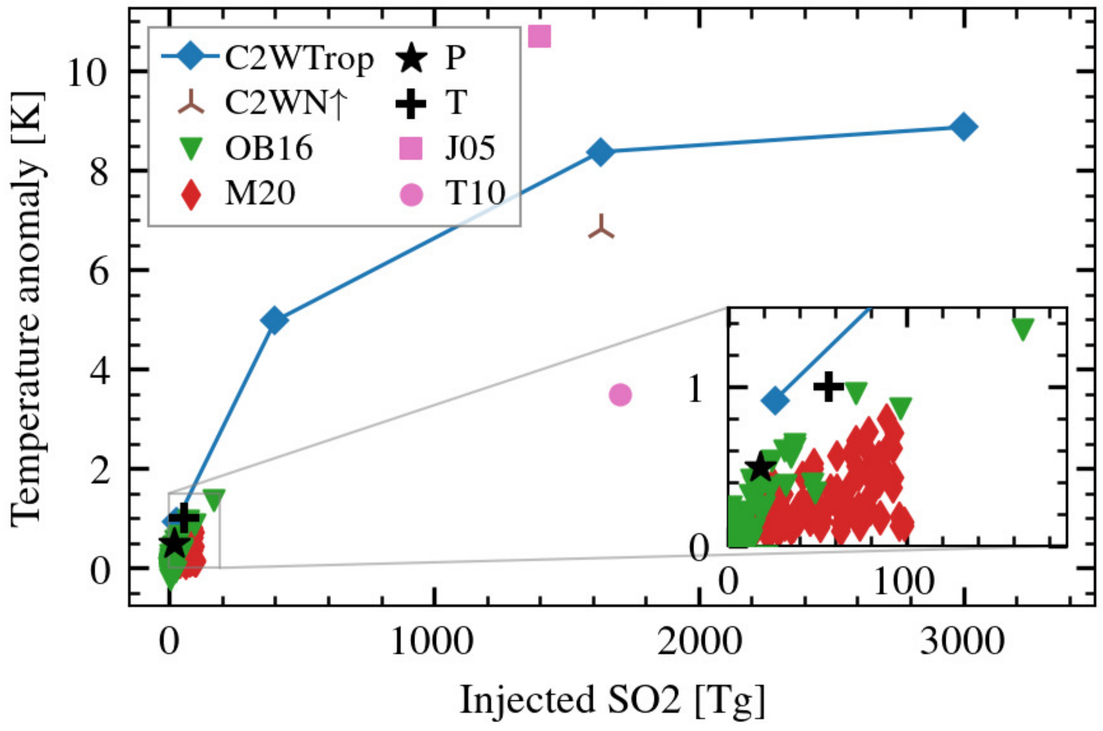
C2WTrop
C2WN↑
OB16
M20
P
T
J05
T10
Temperature anomaly [K]
Injected SO2 [Tg]

(d)

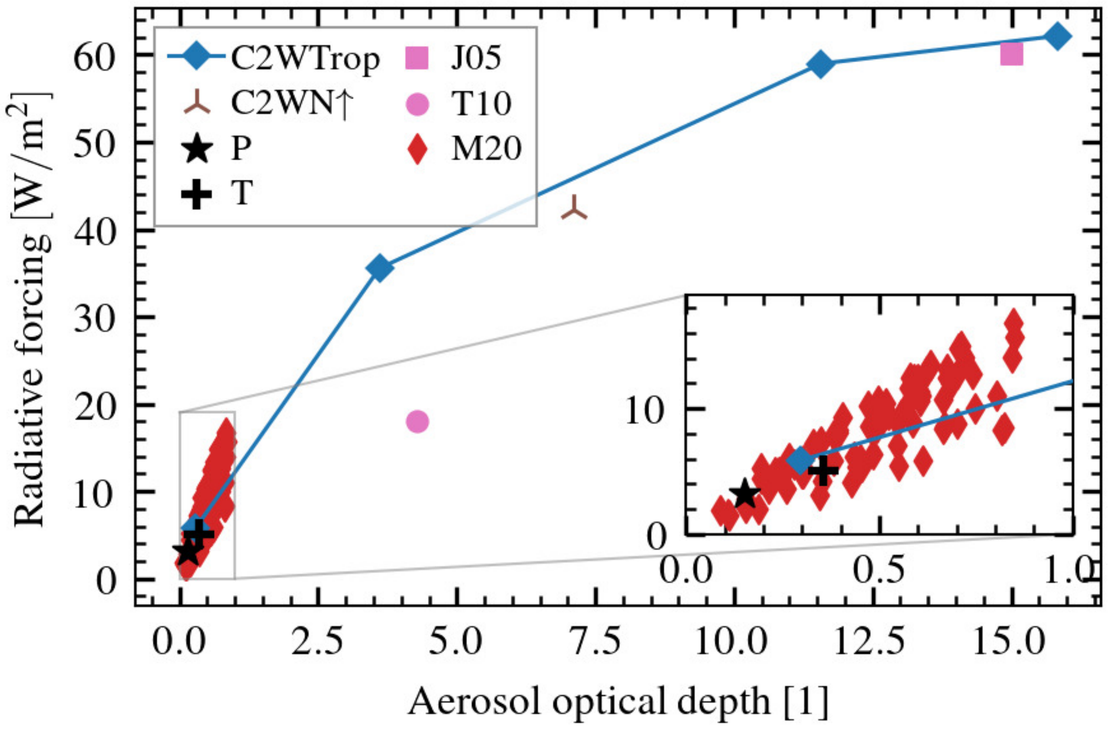
C2WTrop
C2WN↑
P
T
J05
T10
M20
Radiative forcing [W/m^2]
Aerosol optical depth [1]

(e)

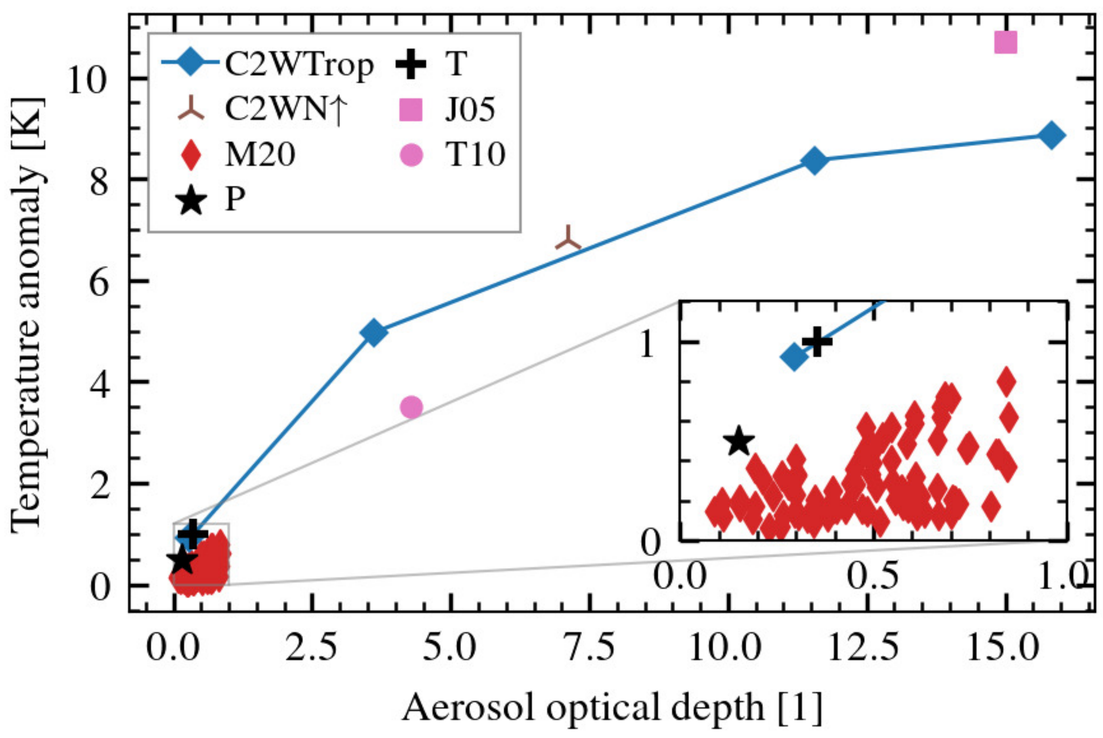
C2WTrop
C2WN↑
M20
P
T
J05
T10
Temperature anomaly [K]
Aerosol optical depth [1]

(f)

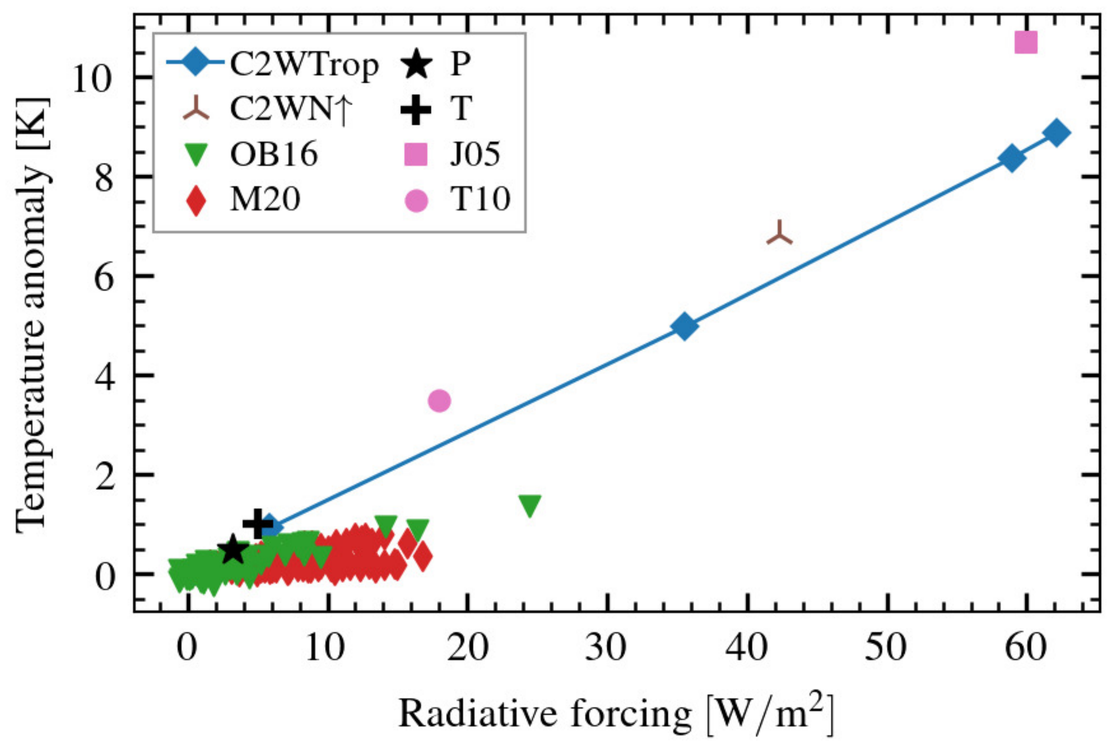
C2WTrop
C2WN↑
OB16
M20
P
T
J05
T10
Temperature anomaly [K]
Radiative forcing [W/m^2]